Available online at www.sciencedirect.com

ScienceDirect

Geochimica et Cosmochimica Acta 323 (2022) 74–101

Geochimica et Cosmochimica Acta

www.elsevier.com/locate/gca

Search for a meteoritic component within the impact melt rocks of the Chicxulub impact structure peak ring, Mexico

Jean-Guillaume Feignon [a,*], Toni Schulz [a,b], Ludovic Ferrière [c], Steven Goderis [d], Sietze J. de Graaff [d,e], Pim Kaskes [d,e], Thomas Déhais [d,e], Philippe Claeys [d], Christian Koeberl [a]

[a] *Department of Lithospheric Research, University of Vienna, Althanstrasse 14, A-1090 Vienna, Austria*
[b] *Institute for Geology and Mineralogy, University of Cologne, Zülpicher Strasse 49b, 50674 Cologne, Germany*
[c] *Natural History Museum, Burgring 7, 1010 Vienna, Austria*
[d] *Research Unit: Analytical, Environmental & Geo-Chemistry, Department of Chemistry, Vrije Universiteit Brussel, AMGC-WE-VUB, Pleinlaan 2, 1050 Brussels, Belgium*
[e] *Laboratoire G-Time, Université Libre de Bruxelles, Av. F.D. Roosevelt 50, 1050 Brussels, Belgium*

Received 31 August 2021; accepted in revised form 3 February 2022; available online 9 February 2022

Abstract

Constraining the degree of preservation of a meteoritic signature within an impact structure provides vital insights in the complex pathways and processes that occur during and after an impact cratering event, providing information on the fate of the projectile. The IODP-ICDP Expedition 364 drilling recovered a ~829 m continuous core (M0077A) of impactites and basement rocks within the ~200-km diameter Chicxulub impact structure peak ring. No highly siderophile element (HSE) data have been reported for any of the impact melt rocks of this drill core to date. Previous work has shown that most Chicxulub impactites contain less than 0.1% of a chondritic component. Only few impact melt rock samples in previous drill cores recovered from the Chicxulub might contain such a signal. Therefore, we analyzed impact melt rock and suevite samples, as well as pre-impact lithologies of the Chicxulub peak ring, with a focus on the HSE concentrations and Re–Os isotopic compositions.

Similar to the concentrations of the other major and trace elements, those of the moderately siderophile elements (Cr, Co, Ni) of impact melt rock samples primarily reflect mixing between a mafic (dolerite) and felsic (granite) components, with the incorporation of carbonate material in the upper impact melt rock unit (from 715.60 to 747.02 meters below seafloor). The HSE concentrations of the impact melt rocks and suevites are generally low (<39 ppt Ir, <96 ppt Os, <149 ppt Pt), comparable to the values of the average upper continental crust, yet three impact melt rock samples exhibit an enrichment in Os (125–410 ppt) and two of them also in Ir (250–324 ppt) by one order of magnitude relative to the other investigated samples. The $^{187}Os/^{188}Os$ ratios of the impact melt rocks are highly variable, ranging from 0.18 to 2.09, probably reflecting heterogenous target rock contributions to the impact melt rocks. The significant amount of mafic dolerite (mainly ~20–60% and up to 80–90%), which is less radiogenic ($^{187}Os/^{188}Os$ ratio of 0.17), within the impact melt rocks makes an unambiguous identification of an extraterrestrial admixture challenging. Granite samples have unusually low $^{187}Os/^{188}Os$ ratios (0.16 on average), while impact melt rocks and suevites broadly follow a mixing trend between upper continental crust and chondritic/mantle material. Only one of the investigated samples of the upper impact melt rock unit could also be interpreted in terms of a highly diluted (~0.01–0.05%) meteoritic component. Importantly, the impact melt rocks and pre-impact lithologies were affected by post-impact hydrothermal alteration processes, probably remobilizing Re and Os. The mafic contribution, explaining the least

* Corresponding author.
E-mail address: jean-guillaume.feignon@univie.ac.at (J.-G. Feignon).

https://doi.org/10.1016/j.gca.2022.02.006
0016-7037/

radiogenic $^{187}Os/^{188}Os$ values, is rather likely. The low amount of meteoritic material preserved within impactites of the Chicxulub impact structure may result from a combination of the assumed steeply-inclined trajectory of the Chicxulub impactor (enhanced vaporization, and incorporation of projectile material within the expansion plume), the impact velocity, and the volatile-rich target lithologies.

Keywords: Chicxulub; Peak ring; Impact melt rocks; Highly siderophile elements; Re-Os isotopes; Meteoritic component

1. INTRODUCTION

The Chicxulub impact structure, ~200-km-in-diameter (Gulick et al., 2013) and 66.05 Myr old (Sprain et al., 2018), is located in the northwestern part of the Yucatán peninsula, Mexico (Fig. 1). The circular structure was identified based on the observation of large-scale negative Bouguer gravity and magnetic anomalies (Hildebrand et al., 1991, and references therein). The identification and characterization of shocked quartz grains in drill core samples from within the structure was used to confirm its impact origin (Hildebrand et al., 1991). Chicxulub is the only known impact structure on Earth with a well-preserved peak ring (e.g., Morgan et al., 2016, and references therein). The structure formed following the oblique impact of a ~12-km-diameter body (Collins et al., 2020) on a target rock made of ~3-km thick, Mesozoic carbonate and evaporite, platform overlying crystalline basement rocks (Lopez Ramos, 1975; Urrutia-Fucugauchi et al., 2011; Morgan et al., 2016). The Chicxulub impact event coincides with the end of the Mesozoic Era, which is marked by the Cretaceous-Paleogene (K–Pg) boundary, and the extinction of, for instance, the non-avian dinosaurs (e.g., Swisher et al., 1992; Smit, 1999; Schulte et al., 2010; DePalma et al., 2019; Chiarenza et al., 2020). The K–Pg impact event is marked in the geologic record by a thin layer of clay, which has, so far, been found in more than 350 terrestrial and marine sites around the world (e.g., Smit, 1999; Claeys et al., 2002; Schulte et al., 2010).

An iridium enrichment several thousand times higher than the average upper continental crust (UCC) value (average composition of Earth's continental crust ~0.02 ppb Ir; Peucker-Ehrenbrink and Jahn, 2001) was first characterized in the K–Pg layer sites of Gubbio (Italy) and Caracava (Spain), leading to the hypothesis of a large impact event as the cause of the mass extinction at the K–Pg boundary

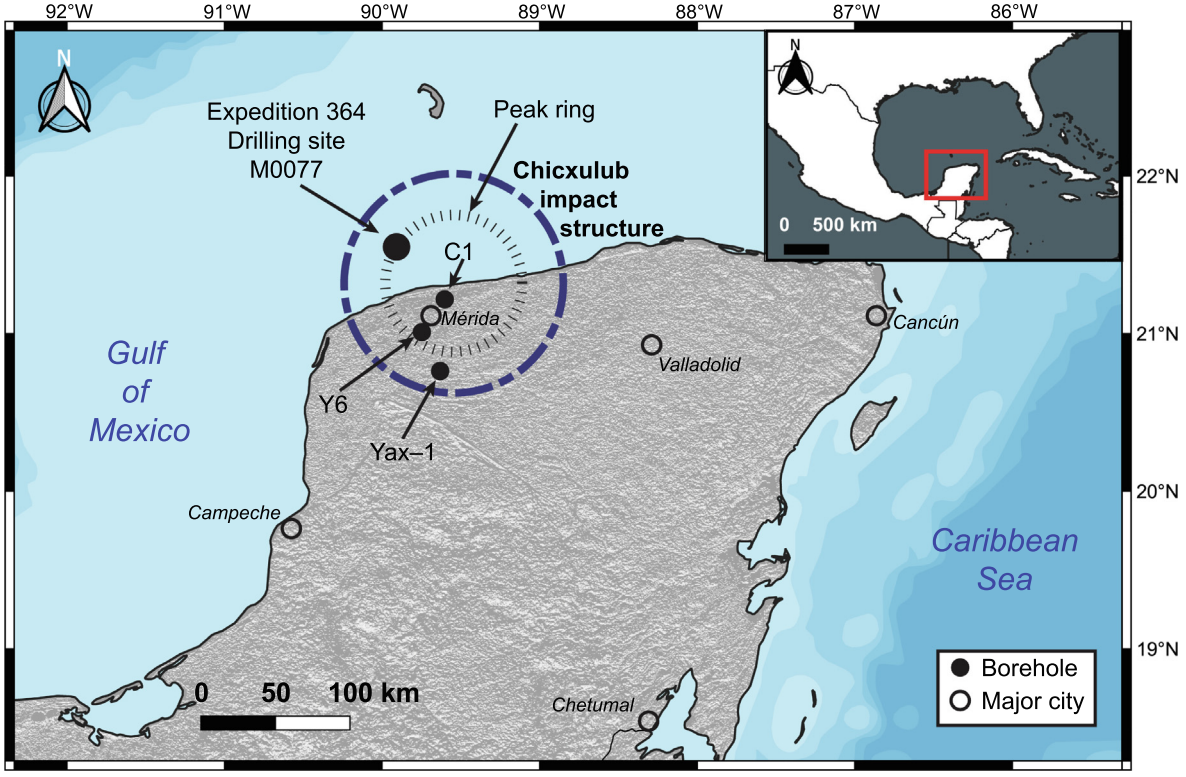

Fig. 1. Map and digital elevation model of the Yucatán peninsula, SE Mexico, showing the 200-km-diameter Chicxulub impact structure (dashed line) and the peak ring (thin circle within). The locations of the M0077A drill core, as well as other drill cores within the impact structure that are discussed in the text, are shown for reference.

(Alvarez et al., 1980; Smit and Hertogen, 1980). Subsequent investigations at other K–Pg boundary sites measured Ir enrichments of up to 87 ppb (Claeys et al., 2002). Enrichments in moderately (e.g., Cr, Co, and Ni), and other highly siderophile elements (Ru, Rh, Pd, Re, Os, Pt, and Au; HSE) were also found at a number of K–Pg boundary sites (see Schulte et al., 2010; Goderis et al., 2013, and references therein). The projectile component in the boundary layer was determined to be of carbonaceous chondritic composition (Kyte, 1998; Trinquier et al., 2006; Quitté et al., 2007; Goderis et al., 2013). Since then, iridium, and, more broadly, the HSE (e.g., Os, Pt) contents, as well as Re–Os isotopic compositions, have been identified as geochemical tracers to reveal a projectile component in ejecta (e.g., Koeberl et al., 2012; Koeberl, 2014). Other impactites, and, more specifically, impact melt rocks can also contain traces of the original projectile (e.g., Palme et al., 1978; Morgan et al., 1979, Tagle and Hecht, 2006; Koeberl et al., 2012; Koeberl, 2014). Such meteoritic material was identified, using the aforementioned geochemical tools, within the large Vredefort impact structure (South Africa) Granophyre, displaying HSE abundances and Re–Os isotopic compositions that can only be explained by the addition of ~0.2% of chondritic material (French et al., 1989; Koeberl et al., 1996). Similarly, an unambiguous meteoritic contribution was identified within the chemically homogeneous impact melt rock body of the Morokweng impact structure (~70–80-km-diameter, South Africa), with an estimated chondritic contribution between ~2 and ~5% (e.g., Koeberl et al., 1997; Koeberl and Reimold, 2003). Additionally, a preserved, 25-cm sized meteorite clast was discovered within the impact melt rocks recovered from a drill core (Maier et al., 2006). In the case of Morokweng, the meteoritic component is relatively abundant and is homogeneously distributed within the impact melt rocks (Koeberl et al., 1997), in contrast to the impact melt rocks from other impact structures (Koeberl, 1998). The average $^{187}Os/^{188}Os$ ratio of the UCC is ~1.4 (Peucker-Ehrenbrink and Jahn, 2001), while undifferentiated meteoritic material (i.e., chondrites) shows significantly less radiogenic $^{187}Os/^{188}Os$ ratios of ~0.12–0.13 (Fischer-Gödde et al., 2010). In addition, chondrites are characterized by elevated HSE abundances, e.g., an average of ~600 ppb Os, ~500–600 ppb Ir, and ~1100 ppb Pt (Horan et al., 2003; Tagle and Berlin, 2008; Fischer-Gödde et al., 2010). Although terrestrial mantle rocks have similarly low $^{187}Os/^{188}Os$ ratios, on the order of ~0.13 (Meisel et al., 2001), their HSE concentrations are at least two orders of magnitude lower compared to chondrites with, e.g., values of ~3.9 ppb Os, ~3.5 ppb Ir, and ~7.6 ppb Pt (Becker et al., 2006). On the other hand, UCC values are ~0.03 ppb Os, ~0.02 ppb Ir, and ~0.51 ppb Pt (Peucker-Ehrenbrink and Jahn, 2001). Consequently, the addition of even a small amount of chondritic material to crustal target rocks associated with a meteorite impact can lead to a significant change of the $^{187}Os/^{188}Os$ signature and the HSE concentrations of the impactites (Walker et al., 2002; Koeberl et al., 2012; Koeberl, 2014, and references therein). However, having a mix of lithologies, including a significant mafic component (or HSE-rich target rock) within the impactites, may simulate a meteoritic component (but requires independent petrographic and/or geochemical confirmation of the presence of such a large mafic component) (see also, Lambert, 1982; McDonald et al., 2007).

Up to now, the presence of a distinct meteoritic component in impactites, comparable to that observed in, for example, Vredefort, Morokweng, or in the East Clearwater Lake (Grieve et al., 1980) impact structures, is rather rare. For the Chicxulub impact structure, several studies came up with mostly a low or heterogeneously distributed meteoritic component within the impactites (Koeberl et al., 1994; Gelinas et al., 2004; Tagle et al., 2004; Tuchscherer et al., 2004a; Goderis et al., 2021). In 2016, the joint International Ocean Discovery Program (IODP) and International Continental Scientific Drilling Program (ICDP) Expedition 364 drilling recovered a ~829 m continuous core (in Hole M0077A) of impactites and basement rocks within the ~200-km diameter (Gulick et al., 2013) Chicxulub impact structure peak ring (Morgan et al., 2016). While an unambiguous meteoritic component was identified in the upper part of the "transitional unit" of the Expedition 364 core (Goderis et al., 2021), the potential presence of a projectile contribution is still to be determined in the impact melt rock units of the core. In order to detect and to constrain the distribution of an extraterrestrial component in rocks forming the Chicxulub peak ring, we have conducted geochemical and isotopic investigations on a selection (n = 33) of impact melt rock, suevite, and pre-impact crystalline lithologies from this drill core, with a specific focus on selected moderately siderophile trace elements (Cr, Co, and Ni), selected HSEs (Re, Os, Ir, and Pt), and Re–Os isotope compositions. The characterization of a wide range of target rock lithologies drilled in this core allows us to identify their respective contributions to the HSE budget and to the Re–Os isotope composition to ascertain whether a meteoritic component is preserved within the impact melt rocks of the peak ring structure. Constraining the degree of preservation of a meteoritic signature within an impact structure provides vital insights in the complex pathways and processes that occur during and after a large impact cratering event.

2. SUMMARY OF PREVIOUS GEOCHEMICAL AND ISOTOPIC WORK ON CHICXULUB AND ITS GLOBALLY DISTRIBUTED EJECTA

The Chicxulub impact structure is buried under ~1 km of Cenozoic limestones, with a ring of cenotes (i.e., water-filled sinkholes) as its only surface expression. Consequently, the direct study of the different lithologies occurring within the impact structure (i.e., a variety of impact breccias, impact melt rocks, and (shocked) pre-impact target rocks), and, thus, the relative abundance of a meteoritic component in these lithologies, relies largely on investigating samples recovered by scientific drilling programs and petroleum exploration campaigns (e.g., Lopez Ramos, 1975; Hildebrand et al., 1991; Koeberl and Sigurdsson, 1992; Kring and Boynton, 1992; Swisher et al., 1992; Koeberl, 1993a; Koeberl et al., 1994; Sharpton et al., 1996; Urrutia-Fucugauchi et al., 1996; Claeys et al., 2003;

Tuchscherer et al., 2004a, and references therein; Belza et al., 2012). Several drilling campaigns were conducted within the impact structure by Petróleos Méxicanos (PEMEX), including Chicxulub–1 (C1) and Yucatán–6 (Y6) cores (Fig. 1), which sampled several impactite units, mainly melt-bearing impact breccias (suevites) and impact melt rocks (e.g., Hildebrand et al., 1991; Kring and Boynton, 1992; Swisher et al., 1992; Schuraytz et al., 1994; Ward et al., 1995; Claeys et al., 2003; Kettrup and Deutsch, 2003); and by the ICDP, recovering the Yaxcopoil–1 (Yax–1) core (e.g., Tuchscherer et al., 2004a, 2004b, 2005, 2006).

Several studies have tried to identify and/or quantify the presence of a meteoritic component within the impactites recovered in C1, Y6, and Yax–1 drill cores. Most of the investigated impact melt rock and suevite samples in the Yax–1 drill core display low Ir contents, generally below 100 ppt, and HSE abundance patterns similar to those of the UCC (Tagle et al., 2004; Tuchscherer et al., 2004a). Clast-rich (with quartz, feldspar, anhydrite, and carbonate clasts) impact melt rock sample Y6-N19 from the Y6 drill core shows similar upper crustal HSE composition (Tagle et al., 2004). In these impactites, the meteoritic component, if present, corresponds to the equivalent of less than 0.05% chondrite (Tagle et al., 2004). Minor enrichments were measured in three samples from Yax–1, i.e., (1) a clast-supported, reworked suevite, with limestone, fossils, and melt fragments at 800.4 m depth in the core, (2) a fine-grained, carbonate groundmass supported suevite containing melt particles at 844.8 m depth, and (3), a polymict impact melt breccia with a fine-grained carbonate groundmass at 890.5 m depth (Tuchscherer et al., 2004a). The Ir contents of these samples are up to ~400 ppt, which is higher by a factor of 50 compared to other impactites from Yax–1 and upper crustal values (Tuchscherer et al., 2004a). These Ir enrichments were thought to be indicative of a minor, heterogeneously distributed, meteoritic signature within the impactites (Tuchscherer et al., 2004a). Other impact melt rock samples from Yax–1 were investigated by Gelinas et al. (2004), revealing variable Os contents, ranging from 11 to 368 ppt, and corresponding $^{187}Os/^{188}Os$ ratios, which range from ~0.19 to ~2.31. These data were interpreted to indicate the presence of a minor and heterogeneously distributed chondritic component, equivalent to less than 0.1% of a chondritic admixture in four samples but less than 0.01% of such a component in nine samples. Only two studies reported elevated Ir contents, potentially indicative of a meteoritic component in C1 and Y6 impact melt rocks. Iridium concentrations of ~6 and ~13.8 ppb, respectively were measured in powder splits (i.e., aliquot from the same prepared powder) from C1 and Y6 impact melt rocks (Koeberl et al., 1994; Schuraytz et al., 1996). The powder split from C1, showing a high Ir content (~6 ppb), also has a high Os concentration of ~25 ppb, associated with a subchondritic $^{187}Os/^{188}Os$ ratio of ~0.11. This was explained as representing an admixture of ~3% of meteoritic material (Koeberl et al., 1994). However, other studies failed to reproduce these anomalies in Y6 and C1 (see also, Tagle et al., 2004, and references therein).

The most compelling evidence of a chemical contamination from the projectile is found in distal K–Pg impact ejecta, including Ir and other HSEs enrichments in the K–Pg clay layer at different sites worldwide (Schulte et al., 2010; Goderis et al., 2013). In a few cases, this analysis was also coupled with Re–Os and Cr isotope compositions that were interpreted to reflect the signature of a carbonaceous chondrite component (Shukolyukov and Lugmair, 1998; Trinquier et al., 2006; Quitté et al., 2007). Notably, a 2.5-mm lithic clast (included in a ~4-mm-sized light-brown clay inclusion), interpreted as an altered carbonaceous chondrite, was found in drill core from Deep Sea Drilling Project (DSDP) Hole 576, which sampled marine K–Pg sediments from the North Pacific Ocean, and is considered to represent material from the Chicxulub projectile (Kyte, 1998). In contrast, the proximal K–Pg ejecta deposits found around the Gulf of México, which are thicker than distal ejecta (i.e., from a few centimeters to tens of meters of clastic beds) and were formed following high-energy sediment transport (tsunami or gravity flows), show a more moderate Ir anomaly due to dilution processes, with an Ir content generally below 1.5 ppb (e.g., Smit, 1999; Claeys et al., 2002; Schulte et al., 2010; Goderis et al., 2013; Sanford et al., 2016). This is similar to the Ir anomaly found at the top of the transitional unit in the Expedition 364 M0077A drill core (Goderis et al., 2021).

3. THE IODP-ICDP EXPEDITION 364 DRILL CORE

The IODP-ICDP Expedition 364 successfully recovered a continuous core between 505.7 and 1334.7 meters below seafloor (mbsf) into the Chicxulub impact structure peak ring (Figs. 1–2a). The drilling took place offshore of the Yucatán peninsula at site M0077A (21.45°N, 89.95°W; Morgan et al., 2017).

The drill core was subdivided in four main lithological units (see Morgan et al., 2017), consisting of: (1) a ~112 m "post-impact" Cenozoic sedimentary rock section (from 505.70 to 617.33 mbsf), further divided in seven lithostratigraphic subunits, with the deepest sub-unit (unit 1G) defined as a ~75-cm thick, fine-grained, and carbonate-rich transitional unit (from 616.58 to 617.33 mbsf) in which the Ir anomaly (~1.0 ppb) was found (Goderis et al., 2021); (2) a ~98 m impact melt-bearing polymict impact breccia (defined as suevite) unit (from 617.33 to 715.60 mbsf), further subdivided in three subunits, i.e., with increasing depth, the bedded suevite (617.33–620.88 mbsf), the graded suevite (620.88–710.01 mbsf), and the non-graded suevite (710.01–715.60 mbsf), according to the classification of the suevite sequence proposed by Kaskes et al. (2022); (3) an ~31 m thick impact melt rock sequence (from 715.60 to 747.02 mbsf), composed of two intermingled, and distinct chemically, impact melt rock phases, i.e., a SiO_2-rich and trachyandesitic black melt, and a CaO-rich green phase, made of mainly secondary clay minerals and sparitic calcite (Morgan et al., 2017; de Graaff et al., 2022; Schulte et al., 2021; Kaskes et al., 2022). The impact melt rock sequence can be subdivided in three subunits, i.e., the upper part, a brecciated

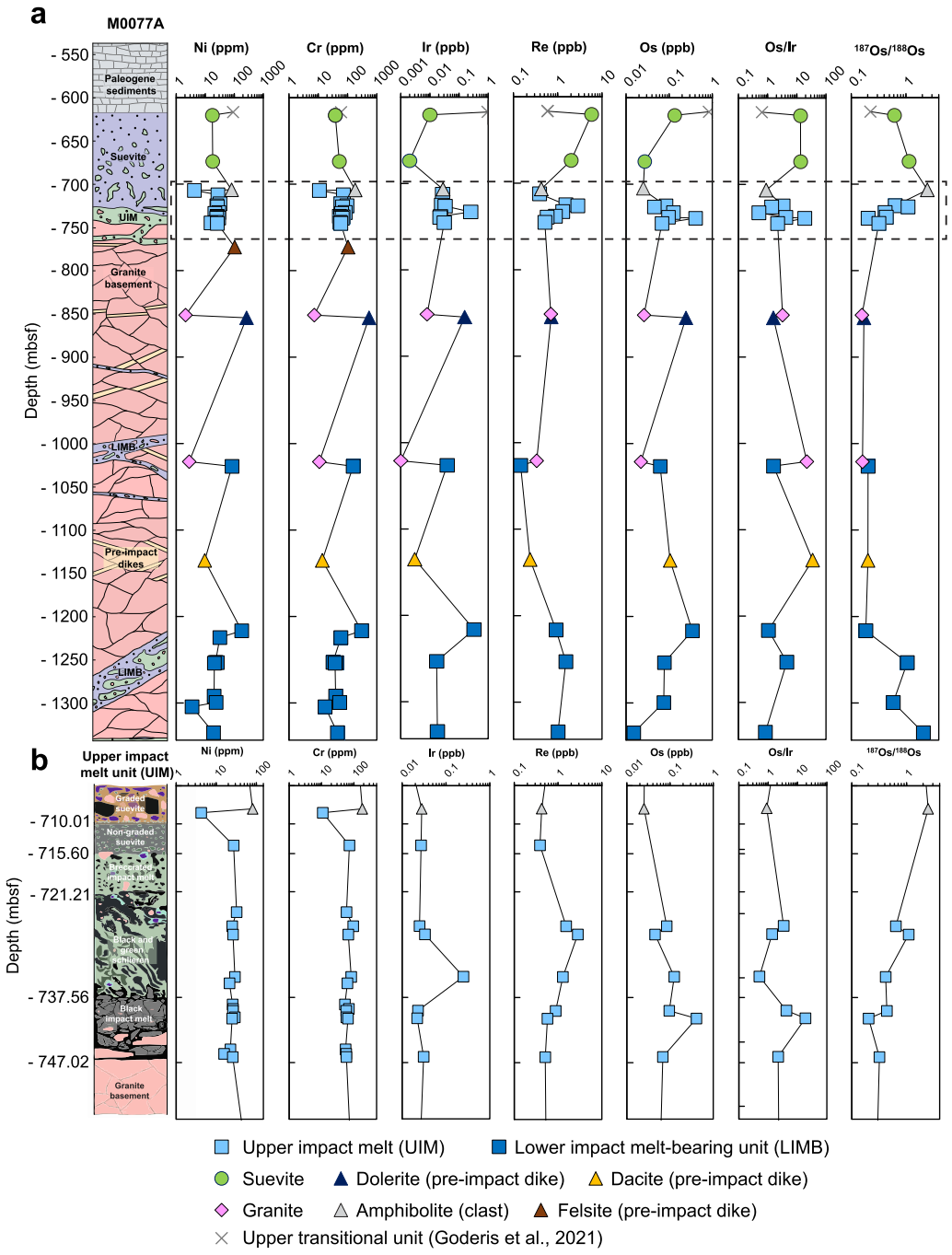

Fig. 2. a) Lithostratigraphy of the M0077A drill core (~550.0–1334.7 mbsf, modified from de Graaff et al., 2022), comparing the concentration variations of selected moderately siderophile elements (Cr and Ni), HSEs (Os, Ir, Re), Os/Ir, and $^{187}Os/^{188}Os$ isotopic compositions with depth in the investigated samples. Cobalt concentrations are varying similarly to Cr, and Ni. Values from the upper transitional unit (Goderis et al., 2021) are shown to highlight the differences in HSE and Os isotopic compositions. The dashed frame represents the UIM interval shown in (b). b) Schematic representation of the main lithological and textural characteristics of the UIM sequence, located above the shocked granite unit (modified from Schulte et al., 2021, with the interval names defined in Kaskes et al., 2022), and showing the same selected elements, elemental ratios, and isotopic composition as in (a).

impact melt rock with angular black impact melt fragments in a green phase matrix (from 715.60 to 721.21 mbsf), then a schlieren texture between both black impact melt rock and the green phase (from 721.21 to 737.56 mbsf), and the lower part of the unit (from 737.56 to 747.02 mbsf) is composed of black impact melt rock only, with the occurrence of crystalline basement clasts (Schulte et al., 2021; de Graaff et al., 2022; Kaskes et al., 2022); and (4), a crystalline basement rock unit (from 747.02 to 1334.69 mbsf) mainly made of shocked, fractured, and deformed,

coarse-grained granite, with locally aplitic and pegmatitic textures. The granite is defined as a high-K calc-alkaline granite; it was shocked at pressures estimated between ~16 and 18 GPa, and undergone both pre- and post-impact pervasive hydrothermal alteration (Feignon et al., 2020, 2021; Kring et al., 2020; Zhao et al., 2020; de Graaff et al., 2022). The granite unit is pervasively intruded by pre-impact subvolcanic dikes, including dolerite, felsite, and dacite, as well as by impact-related dikes (i.e., impact melt rock and impact melt rock-bearing breccia; Morgan et al., 2017; de Graaff et al., 2022). These impact-related dikes are more abundant in the lower part of the granite unit, between 1206.98 to 1334.69 mbsf, and display varying degrees of brecciation and deformation.

In this study we use the four units mentioned above, as defined in Morgan et al. (2017), with units (2) and (3) representing the "upper peak ring" section, while the unit (4) represents the "lower peak ring" section. The subunits used for the "upper peak ring" section are those described in Kaskes et al. (2022). The impact melt rock samples comprise impact melt rock clasts located in the suevite unit (2) described in Kaskes et al. (2022), samples from the upper impact melt rock (UIM) unit (3) as presented in de Graaff et al. (2022), and samples from the lower impact melt rock-bearing unit (LIMB), with all the impact melt rock and impact melt rock-bearing units found in the granite unit (4) considered to be part of the LIMB, as in de Graaff et al. (2022).

Previous work on impact melt rocks from the Hole M0077A drill core showed that they have mainly an andesitic composition (54.4–71.7 wt.%), resulting from the mixing and melting of mafic and felsic target rock compositions, with the dolerite and granitoid possibly representing the major components, in addition to varying degrees of carbonate admixture (de Graaff et al., 2022). While the LIMB shows no indication of carbonate dilution, the UIM is characterized by the presence of a carbonate component, as well as undigested carbonate clasts (de Graaff et al., 2022). The origin of the LIMB is debated with de Graaff et al. (2022) interpreting it as impact melt rock that has been injected into the crystalline target rock during the first phases of crater formation (compression and excavation stages) and that then brecciated after the central uplift collapse. In contrast, Riller et al. (2018) proposed that the LIMB was emplaced at the end of the peak ring formation, following entrainment and trapping of melt bodies within target rock thrust zones.

So far, meteoritic matter was only found in the upper part of the so-called "transitional unit", where a thin gray-green marlstone layer (616.55–616.58 mbsf) was identified, below the Danian pelagic limestone (Lowery et al., 2018; Gulick et al., 2019; Whalen et al., 2020). The interval between 616.55 and 616.58 mbsf is characterized by significant enrichments in Ni (50–100 ppm), Ir (~1.0 ppb), and HSEs (Os, Ru, Pt, and Pd), in addition to lower initial $^{187}Os/^{188}Os_i$ ratio (0.224–0.250) when compared to the lower part of the "transitional unit" (0.281–0.367) and the UCC values (Table 1; Goderis et al., 2021). The meteoritic contribution in the gray-green marlstone layer is estimated at ~0.1% chondritic (Goderis et al., 2021).

4. ANALYTICAL METHODS

Samples with masses ranging from ~20 to 50 g were crushed in polyethylene wrappers and then powdered in an agate bowl using a Retsch RS200 vibratory disc mill at the University of Vienna. Macrophotographs of the main sample types investigated are presented in Fig. 3. Details on sample material, i.e., petrographic descriptions, and major element compositions, can be found in the Supplementary Material.

4.1. Trace element analysis

Trace element concentrations (including Cr, Co, and Ni) were measured using bulk XRF as well as Instrumental Neutron Activation Analysis (INAA). The bulk XRF measurements for trace element concentrations were done on pressed powder pellets. Sample preparation and measurement was done following the methodology described in Feignon et al. (2021). The international reference material used for bulk XRF trace element concentration calibration was GSR 1–6 (Xie et al., 1989).

For bulk INAA analysis, international reference materials used were Ailsa Craig granite AC-E (Centre de Recherches Pétrographiques et Géochimiques, Nancy, France), the carbonaceous chondrite Allende (ALL; Smithsonian Institution, Washington DC, USA), and the Devonian Ohio shale SDO-1 (USGS). The reproducibility for trace elements is on the order of ~2–15% relative standard deviation. The details on instrumentation, accuracy, and precision of this method are given in, e.g., Koeberl (1993b), Son and Koeberl (2005), Mader and Koeberl (2009), Feignon et al. (2021), and references therein.

4.2. Micro-X-ray fluorescence

In addition to the bulk powder geochemical techniques, we applied energy-dispersive micro-X-ray fluorescence (μXRF) mapping of 17 polished thick sections in order to get a better understanding of the distribution of major and trace elements (specifically Ni, Cr, and Co) within the different Chicxulub impactite and target lithologies and to investigate whether specific mineral phases are enriched in moderately siderophile elements and thus a potential meteoritic signature. For this, an M4 Tornado benchtop μXRF surface scanner (Bruker Nano GmbH, Berlin, Germany) equipped with a Rh tube as X-ray source and two XFlash 430 Silicon Drift detectors was used at the Vrije Universiteit Brussel, Belgium (VUB). The μXRF mapping was performed under near-vacuum conditions (20 mbar), using both detectors at maximized X-ray source energy settings (50 kV and 600 μA) and with a spot size and spatial resolution of 25 μm in combination with an integration time of 5 ms per pixel. For the first major element measurement run no specific X-ray source filter was applied, but to enhance the visualization of moderately siderophile elements such as Cr, Co, and Ni, an Aluminum 630 μm filter was applied during a second mapping. This filter allows for a more sensitive detection of trace elements by reducing the X-ray signal for lighter major elements such as Al, Si,

Table 1
Summary table with average moderately and highly siderophile elements, and Os isotope data of investigated samples from this study and from the available literature on the IODP-ICDP Expedition 364 (M0077A Hole) drill core, as well as from previous cores (i.e., Yax–1, Y6, and C1) from the Chicxulub impact structure. Outlier impact melt samples are also presented. n/a: not available, n.d.: non detectable, (?) ambiguous.

Sample group (site or core; lithology)	Cr (ppm)	Co (ppm)	Ni (ppm)	Re (ppb)	Os (ppb)	Ir (ppb)	Pt (ppb)	($^{187}Os/^{188}Os$)	Range of meteoritic contribution (%)
M0077A core									
Average green marlstone (Goderis et al., 2021; n = 3)	24.7	8.01	68.0	0.32	0.82	1.27	3.87	0.23	<0.05–0.1%
Average transitional unit (Goderis et al., 2021; n = 27)	17.0	11.3	38.9	0.69	0.44	0.27	2.23	0.28	~0.05%
Average suevite (n = 2)	45.3	10.6	17.8	3.90	0.08	0.006	0.08	0.88	<0.01%
Average UIM (n = 15)	61.5	13.4	24.1	1.14	0.14	0.06	0.10	0.52	n.d.–0.05%
91R1_102–104.5*	82.3	15.6	29.2	1.29	0.13	0.25	0.10	0.42	~0.01–0.05%
93R2_11–12.5*	65.4	14.3	24.8	0.57	0.41	0.02	0.08	0.20	~0.1%(?)
Average LIMB (n = 10)	77.9	20.7	43.1	0.90	0.11	0.10	0.15	0.82	n.d.–0.1%(?)
265R2_9–11*	299	58.2	180	0.82	0.34	0.32	0.35	0.18	~0.1%(?)
Average dolerites (n = 1)	542	68.3	266	0.71	0.25	0.16	0.35	0.17	n.d.
Average amphibolites (n = 1)	181	32.4	81.0	0.42	0.03	0.03	0.21	2.47	n.d.
Average felsites (n = 1)	105	26.2	103	n/a	n/a	n/a	n/a	n/a	n.d.
Average dacites (n = 1)	13.7	8.22	9.60	0.24	0.11	0.003	0.04	0.20	n.d.
Average granites (n = 2)	9.10	2.30	2.45	0.52	0.02	0.005	0.09	0.16	n.d.
Yax-1 core									
Suevites (Tagle et al., 2004; n = 5)	55.2	15.0	17.8	n/a	n/a	0.06	0.52	n/a	<0.05%
Impactites (Tuchscherer et al., 2004a; n = 43)	42.0	7.09	21.2	n/a	n/a	<0.4	n/a	n/a	<0.1%
Impactites (Gelinas et al., 2004; n = 16)	n/a	n/a	n/a	0.06	0.10	n/a	n/a	0.63	<0.01–0.1%
Y6 core									
Y6-N19 Impact melt sample (Schuraytz et al., 1996; Tagle et al., 2004)	15	42	15	n/a	n/a	0.06–13.8	0.45	n/a	<0.01–3%
C1 core									
Data from Koeberl et al. (1994), n = 2	114	14.8	40.0	1.28	12.6	6.00	n/a	0.31	0.01–5%
K-Pg boundary clays									
Data from Goderis et al. (2013)	111	46.2	199	n/a	n/a	5.96	10.2	n/a	~0.1–>5%
Data fromQuitté et al. (2007), n = 11)	n/a	n/a	n/a	7.38	9.31	n/a	n/a	0.22	<0.05–>5%
Fossil meteorite (Kyte, 1998)	6540	76.0	1370	n/a	n/a	690	n/a	n/a	n/a

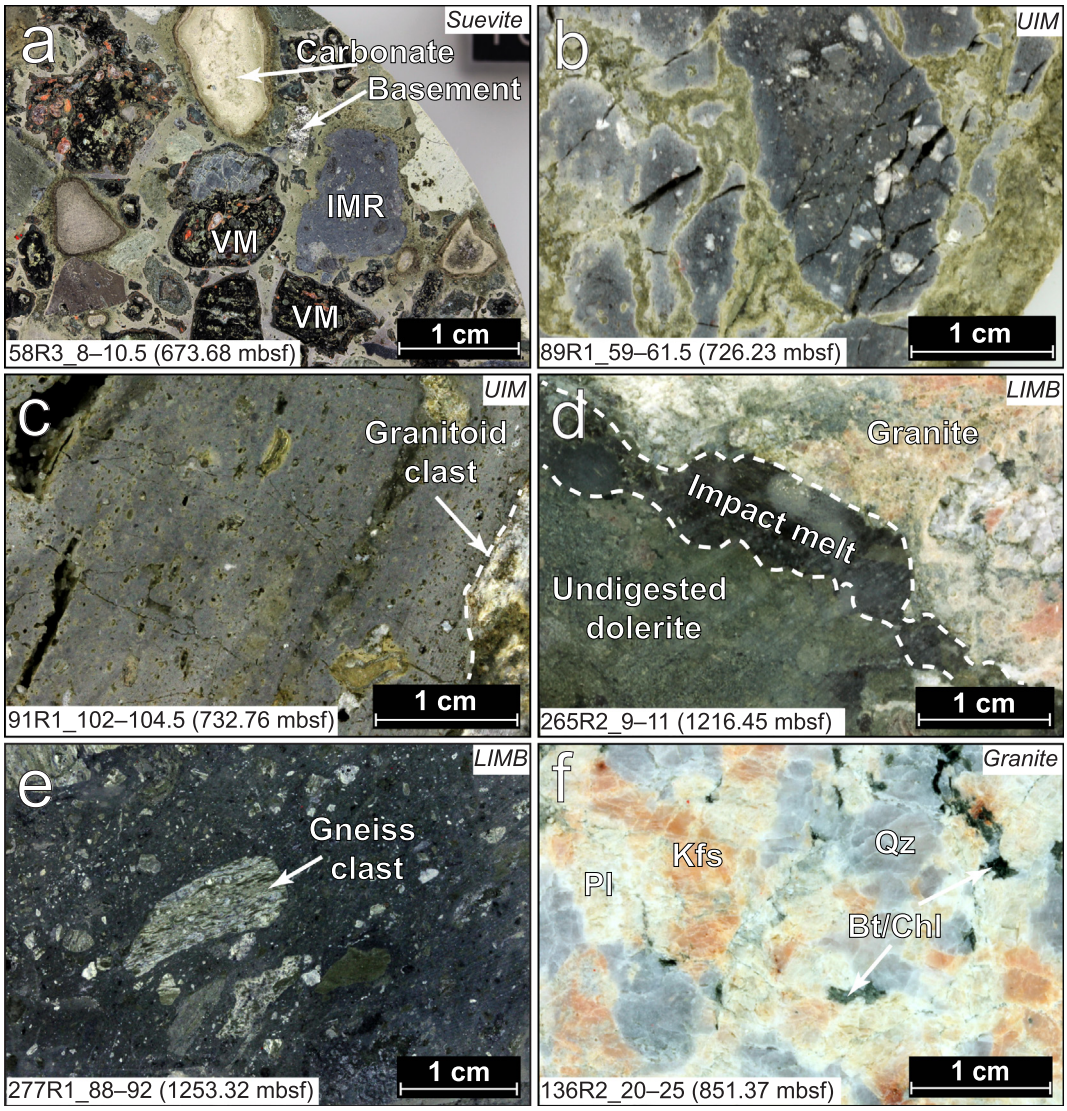

Fig. 3. Macrophotographs of the main sample types encountered. a) Suevite sample from the graded suevite unit (Kaskes et al., 2022) showing several types of centimeter-sized clasts, i.e., carbonates, impact melt rock (IMR), altered vitric melt (VM), and crystalline basement, embedded in a clastic matrix. b–c) Upper impact melt rock samples, with (b) showing the schlieren texture between mingled black impact melt rock and the carbonate-rich, altered, green phase, as well as abundant open fractures crosscutting the sample, and (c) a black melt rock-dominated sample with greenish altered area, clast-poor and vesiculated. A large centimetric granitoid clast is visible on the right side. d–e) Lower impact melt-bearing unit samples, with (d) a relatively thin impact melt intruding at the contact between the granite unit and a dolerite dike, leading to the partial melting of the dolerite, and (e) relatively clast-rich impact melt rock with a large sub-angular gneiss clast. f) Typical coarse-grained granite (pre-impact lithology), relatively undeformed and with limited fracturing, exhibiting the typical paragenesis (i.e., Kfs: K-feldspar, Qz: quartz, Pl: plagioclase, Bt: biotite, and Chl: chlorite). Additional macrophotographs of other pre-impact lithologies are shown in Fig. S1.

Ca, and K (de Winter and Claeys, 2017). This combined approach resulted in qualitative multi-element maps and semi-quantitative single-element heatmaps for a range of elements, in which the highest X-ray intensity for the elements' Kα-line corresponds to the pixel in the sample with the highest possible red-green-blue value (i.e., 255; Kaskes et al., 2021). To correctly visualize the distribution of Co, a peak deconvolution was applied in the M4 Bruker software to overcome the overlap between the Kα peak of Co and the Kß peak of Fe (at 6.93 and 7.06 keV, respectively).

4.3. HSE concentrations and $^{187}Os/^{188}Os$ analysis

About ~0.4 to ~0.6 g of homogenized sample powder was spiked with a mixed tracer solution composed of ^{185}Re, ^{190}Os, ^{191}Ir, and ^{194}Pt isotopes and digested in 5 ml acid mixture (HNO_3-HCl: 3 + 2 ml) at 270 °C and 100–130 bars in an Anton-Paar high pressure asher for 5 h. After digestion, Os was separated from the other HSEs using a CCl_4/HBr liquid extraction procedure (Cohen and Waters, 1996). Osmium was further purified using a H_2SO_4/H_2CrO_4 microdistillation technique (Birck et al.,

1997). After Os extraction, all other HSEs were separated by ion-exchange chromatography using the procedure outlined in Pearson and Woodland (2000).

Measurements of Os concentrations and $^{187}Os/^{188}Os$ ratios were carried out at the Department of Lithospheric Research at the University of Vienna, Austria. Osmium was loaded as a bromide on Pt filaments covered with a $NaOH/Ba(OH)_2$ activator (Völkening et al., 1991; Creaser et al., 1991). Analyses were performed using a ThermoFinnigan Triton Thermal Ionization Mass Spectrometer (TIMS), operating in negative ion mode. Isobaric interferences attributable to W- or Pt-oxides were not observed. Isobaric interferences of ^{187}Re on ^{187}Os were monitored by measuring $^{185}ReO_3^-$ (mass 233) and corrected if observed. Mass fractionation was corrected offline using $^{192}Os/^{188}Os = 3.083$ (Brandon et al., 2005; Luguet et al., 2008). The Os total procedural blank was ~0.4 pg (n = 2) contributing less than 0.5% to the measured Os concentrations of the samples.

Repeated Negative-TIMS measurements (n = 3) of 10 pg loads of a DROsS (Durham Romil Osmium Standard) solution were performed using the electron multiplier at signal intensities that were typically achieved during the sample runs (~1,000 to ~100,000 counts on mass 240 = $^{192}OsO^{-3}$). The DROsS measurements yielded an average of 0.16088 ± 56 for $^{187}Os/^{188}Os$, 1.2167 ± 40 for $^{189}Os/^{188}Os$, and 1.9782 ± 80 for $^{190}Os/^{188}Os$ ratios (errors refer to the last two digits). These values agree within the 2σ uncertainty of the average values reported by Luguet et al. (2008), obtained for much larger Os loads of DROsS. The long-term external reproducibilities are ± 0.4% for $^{187}Os/^{188}Os$, ± 0.2% for $^{189}Os/^{188}Os$, and ± 0.3% for $^{190}Os/^{188}Os$ ratios.

Rhenium and HSE concentrations were measured using a Thermo Fisher Element XR ICP-MS in single collector mode at the Steinmann Institute at the University Bonn, Germany, using methods described in Luguet et al. (2015). Instrumental drift was monitored using a 1 ppb in-house multi-element HSE standard solution measured at the beginning, middle, and end of the analytical session. Mass bias was corrected relative to this standard solution using ratios of 0.5986 for $^{185}Re/^{187}Re$, 0.5957 for $^{191}Ir/^{193}Ir$ and 0.2117 for $^{198}Pt/^{195}Pt$ and corrections were insignificant for all samples. Additionally, isobaric interferences caused by Hf on Ir and Pt were monitored and corrected for offline. To determine the oxide production, Hf-doped 1 ppb HSE solutions were run at the beginning, middle, and end of each analytical session. Rhenium, Ir, and Pt were measured using a cyclonic borosilicate glass spray chamber. Total procedural blanks for this study (n = 2) were 3–4 pg for Re, 0.5–1 pg for Ir, and 10–30 pg for Pt. Blank correction for procedural blank is achieved by direct subtraction of the blank contribution from the gross amount of analyte detected. Due to the often very low HSE contents of the analyzed samples, blank corrections were applied in all cases. With respect to individual samples, these blanks resulted in variable uncertainties for the calculated concentrations in the range of <1–30% for Re, 1–60% for Ir, and 1–70% for Pt (highest uncertainties for low HSE dacite (238R1_101–103.5), granites (136R2_20–25 and 200R3_12.5–15), and amphibolite (80R2_61–63.5) samples. Analytical quality was monitored with repeated measurements of reference materials UB-N (lherzolite; Meisel et al., 2003) and OKUM (komatiite; Potts and Meisel, 2015) processed alongside the samples. All analyses of reference materials reproduce certified values within 2σ error.

5. RESULTS

5.1. Moderately siderophile element variations

Concentrations for the moderately siderophile elements, i.e., Cr, Co, and Ni contents are presented in Fig. 4, together with values for the "transitional unit" (Goderis et al., 2021), K–Pg clays (Goderis et al., 2013), and previously investigated granites (Feignon et al., 2021), for comparison. Chromium, Co, and Ni contents all plot between two endmembers, i.e., the granite with the lowest measured Cr, Co, and Ni concentrations (i.e., with 7.3–10.9, 1.90–2.69, and 2.10–2.80 ppm, respectively), and the dolerite which by far shows the highest Cr, Co, and Ni contents, with 542, 68.3, and 266 ppm, respectively. The Cr, Co, and Ni contents of others lithologies, i.e., impact melt rocks, suevites, amphibolite, dacite, and felsite, broadly spread between these two endmembers, with a strong linear correlation observed between all samples (correlation factor $R^2 = 0.95$ for Ni versus Cr, and $R^2 = 0.93$ for Ni versus Co). In most of the impact melt rock and suevite samples, the Cr, Co, and Ni contents show a relatively narrow range, of 22.5–25, 9.68–20.0, and 15.7–32.2 ppm, respectively. Two impact melt rock samples, i.e., 80R2_126–128 impact melt clast, and 294R1_67.5–70 from the LIMB, have moderately siderophile element contents similar to the granites, with 10.9 ppm Cr, 7.48 ppm Co, and 4.20 ppm Ni, and 17.0 ppm Cr, 7.76 ppm Co, 3.50 ppm Ni, respectively. Two other impact melt rocks from the LIMB, i.e., 202R2_48.5–53 and 265R2_9–11, are relatively enriched in Cr, Co, and Ni, in comparison to the other impact melt rocks, with 155 ppm Cr, 25.2 ppm Co, and 83.7 ppm Ni, and 299 ppm Cr, 58.2 ppm Co, and 180 ppm Ni, respectively. The amphibolite has a composition similar to the LIMB sample 202R2_48.5–53 with 181 ppm Cr, 32.4 ppm Co, and 81.0 ppm Ni, while the felsite is slightly enriched in Ni, relative to Cr and Co (see Fig. 4c) with 105 ppm Cr, 26.2 ppm Co, and 103 ppm Ni. On the other hand, the dacite displays lower contents of Cr, Co, and Ni, albeit higher than for the granites, with 13.7, 8.22, and 9.60 ppm, respectively. Generally, the transitional unit samples (Goderis et al., 2021) are depleted in Cr (average of 17.3 ppm) but show similar Co contents (average 10.6 ppm), relative to the investigated samples (Fig. 4 and Table 1). In contrast, the transitional unit samples investigated in Goderis et al. (2021) show a distinct enrichment in Ni (average of 68 ppm) relative to most of the samples investigated here (Fig. 4 and Table 1). The Cr/Ni of impact melt rocks ranges between 1.41 and 4.85 (with an average of 2.43), which is significantly higher than the Cr/Ni for CI-chondrite material, i.e., ~0.26 (Tagle and Berlin, 2008), and close to average UCC values (~2.0; Rudnick and Gao, 2014, and references therein). Importantly, the Cr/Ni and Cr/Co ratios of the investigated impact melt rocks

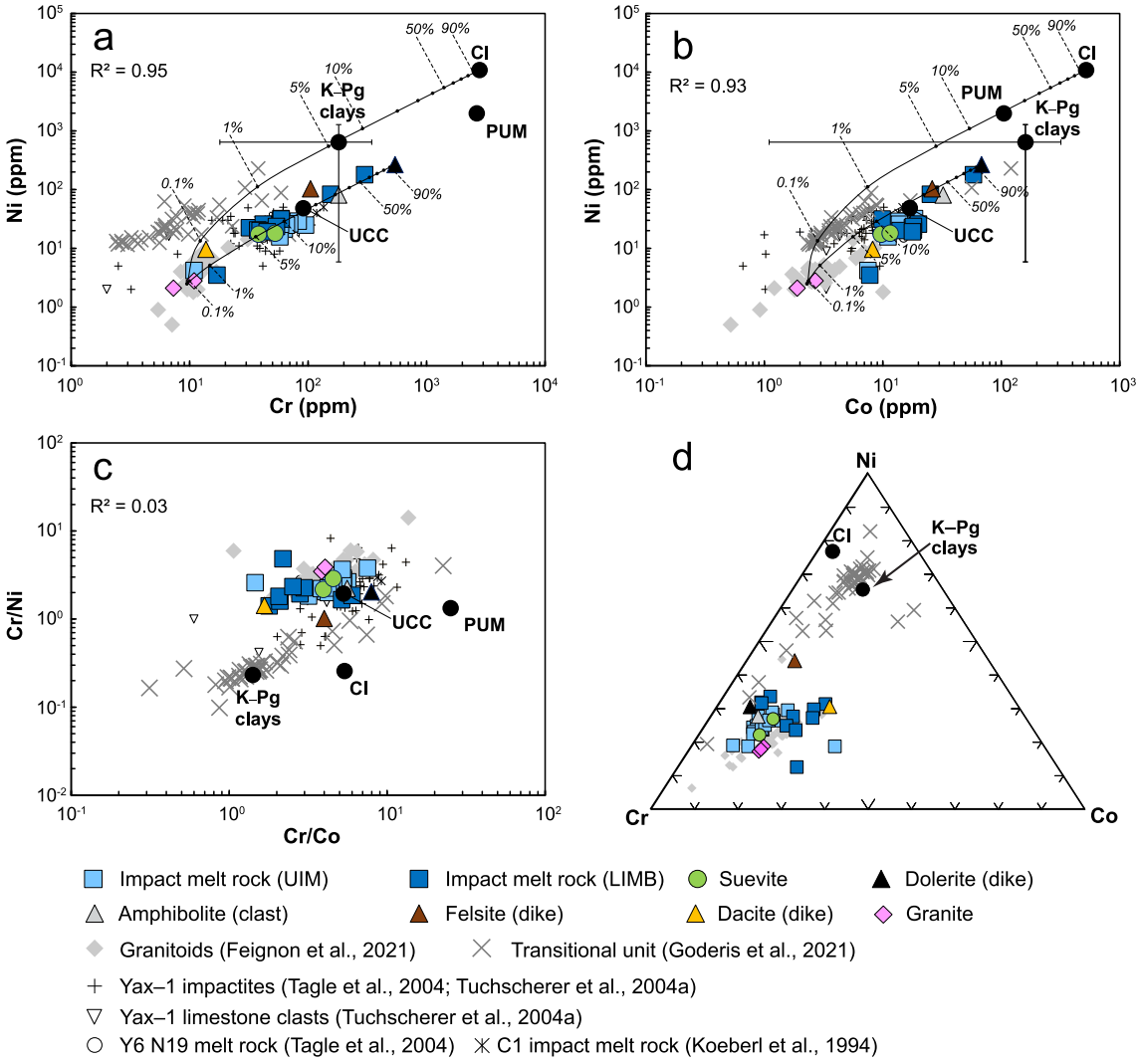

Fig. 4. a–d) Content of the investigated samples for moderately siderophile elements (Cr, Co, and Ni). For comparison, the Ni, Cr, and Co compositions of samples from granitoids as well as the transitional unit (M0077A drill core), and other drill cores were included. The average compositions of K–Pg clays (taking into account the slight variation between proximal and distal sites), CI-chondrites (CI), and primitive upper mantle (PUM), are from Goderis et al. (2013), Tagle and Berlin (2008), and Lubetskaya and Korenaga (2007), respectively. a–b) Bivariate diagrams of Ni versus Cr, and Ni versus Co. All the samples display strong covariations with R^2 above 0.9. Mixing lines are drawn between (1) average granite and CI-chondrite compositions and (2) average granite and dolerite compositions. All the investigated samples broadly follow the mixing line (2). c) Interelement ratio diagram of Cr/Ni versus Cr/Co. d) Ternary diagram of Cr, Ni, and Co, highlighting the Ni-enrichment occurring in the transitional unit samples.

and suevites plot between the pre-impact lithologies compositions, without any sample displaying a composition close to the CI-chondrite component. Six LIMB samples plot between the granite and the dacite compositions, the latter having a higher Co content, and thus, a lower Cr/Co (1.67) than the granite (3.85–4.05). The granites show relatively low Cr, Co, and Ni contents, of 5.40–30.9, 0.50–10.1, and 0.5–14.2 ppm, respectively (this study and Feignon et al., 2021), compared to the average UCC composition (Fig. 4; Rudnick and Gao, 2014, and references therein).

5.2. Micro-X-ray fluorescence

The distribution of the most important major and trace elements (±ppm level) is visualized in the μXRF maps of Fig. 5. Polished thick sections were scanned of which bulk powder data was available, resulting in a representative sample set of two suevites, one amphibolite, seven UIM samples, one dolerite, one dacite, and five LIMB samples (Fig. 5a). The major element trends are shown in an Fe-Si-Ca-K multi-element map and a single-element Ca heatmap (Fig. S5). Suevite and UIM samples are clearly enriched in Ca, present as carbonate clasts, sparry calcite (green schlieren), and calcite veins. The amphibolite, dolerite, dacite, and LIMB samples are depleted in Ca and yield, in general, more Fe-rich phases. The single-element heatmaps of the moderately siderophile elements Cr, Co, and Ni (measured with an Al 630 μm X-ray source filter) are shown in Fig. 5b–d and display clear enrichments in these three elements in amphibolite (80R2_61–63.5), dolerite

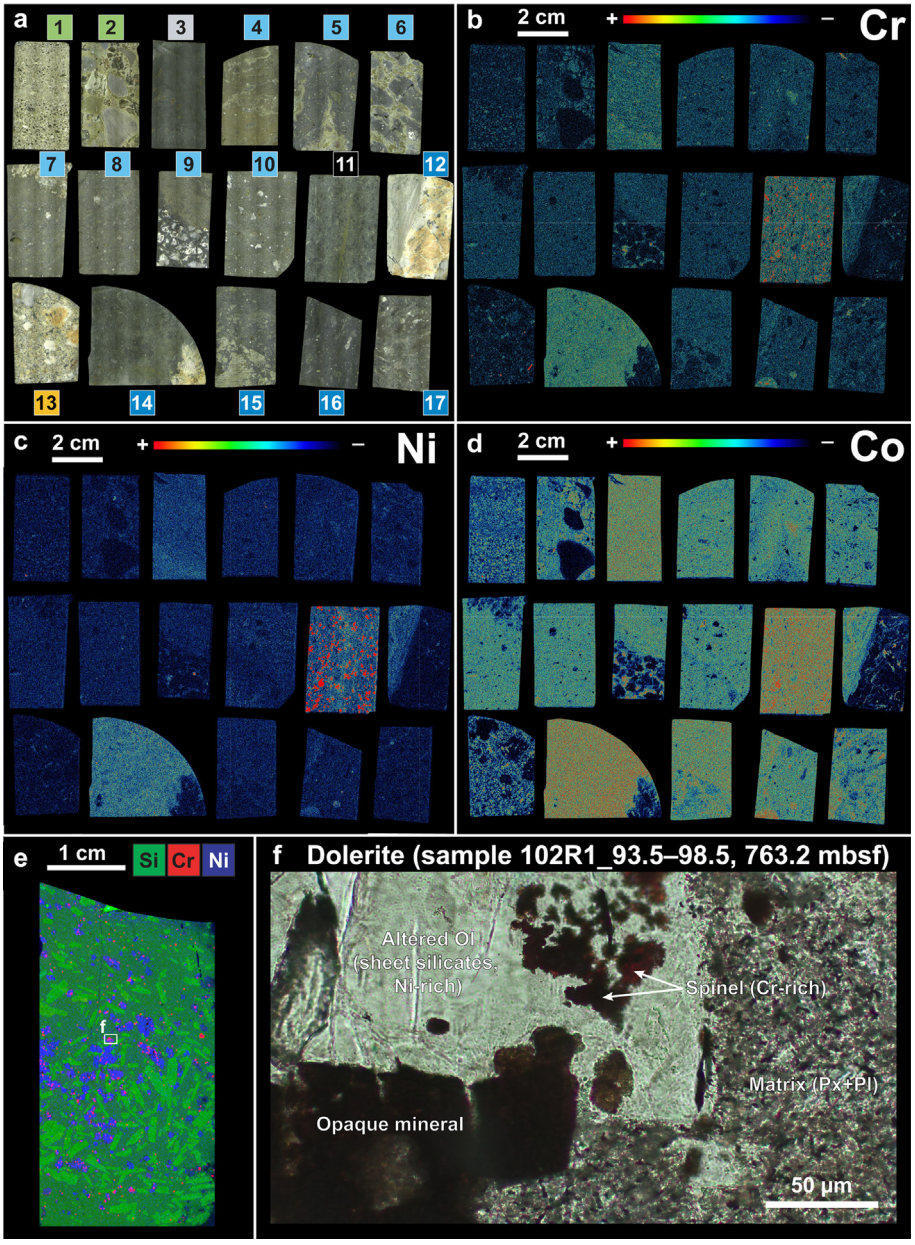

Fig. 5. High-resolution micro-X-ray fluorescence (µXRF) mapping results. a) Scanned image overview of the 17 M0077A impactite and target lithology samples, from upper left to lower right: two suevites, one amphibolite, seven UIM samples, one dolerite, one LIMB, one dacite, and four LIMB samples. Sample details are indicated below. b-d) Single-element distribution maps (or 'heatmaps') of Cr, Co, and Ni, measured using an Al-630 µm X-ray source filter and peak deconvolution applied on the Co map. e) Multi-element map showing the distribution of Si, Cr, and Ni within dolerite sample 102R1_93.5–98.5 (763.2 mbsf). The colors allow to distinguish the different mineral phases forming the dolerite, i.e., plagioclase (light green), altered olivine (blue), spinel-group and opaque minerals (red). The dark green represents the dolerite matrix. Nickel (and Co) are mainly concentrated in altered olivine, while Cr is concentrated in spinel-group minerals. f) Thin section microphotograph (plane polarized light) of dolerite sample shown in Fig. 5e, showing the Ni, Cr, and Co carrier mineral phases. Ol: olivine, Px: pyroxene, and Pl: plagioclase. Sample details with sample ID, lithology/unit, and core depth: 1) 41R1_106–108 (bedded suevite unit, 620.4 mbsf); 2) 53R3_6–8 (graded suevite unit, 673.7 mbsf); 3) 80R2_61–63.5 (amphibolite, 706.6 mbsf); 4) 83R1_22–24.5 (UIM, 712.3 mbsf); 5) 88R3_45–47.5 (UIM, 724.9 mbsf); 6) 89R1_59–61.5 (UIM, 726.2 mbsf); 7) 91R1_102–104.5 (UIM, 732.8 mbsf); 8) 93R1_21–23.5 UIM, 738.1 mbsf); 9) 93R2_11–12.5 (UIM, 739.1 mbsf); 10) 95R2_45–47.5 (UIM, 745.3 mbsf); 11) 140R2_5–8 (dolerite, 854.6 mbsf); 12) 202R48.5–53 (LIMB, 1026.3 mbsf); 13) 238R1_101–103.5 (dacite, 1135.1 mbsf); 14) 265R2_16–19 (LIMB, 1216.6 mbsf, from the same LIMB dike as sample 265R2_9–11); 15) 277R1_88–92 (LIMB, 1253.3 mbsf); 16) 292R2_66–68.5 (LIMB, 1299.4 mbsf); 17) 303R3_22.5–25 (LIMB, 1334.4 mbsf).

(140R2_5–8), and LIMB (265R2_16–19) samples, compared to the other samples. Ni and Cr hotspots in the dolerite sample overlap with enrichments in Mg (not shown here) and – in combination with petrographic analysis – these Ni rich phases are linked to altered olivine minerals, while the Cr-rich phases are linked to spinel group and opa-

que minerals (see Fig. 5e-f). For the other samples, the enrichments in Ni, Cr, and Co show a uniform pattern and, therefore, cannot be associated with any specific mineral phase.

5.3. Highly siderophile element concentrations

Chondrite-normalized highly siderophile element (HSE) abundance patterns (Os, Ir, Pt, and Re) are presented in Fig. 6. Concentrations of the HSE are shown in Fig. 7 and provided in Table 2. The Ir and Os contents of the impact melt rocks (i.e., both UIM and LIMB) are generally relatively low, ranging from 17 to 39 ppt, and 15 to 96 ppt, respectively, similar to the average UCC composition (i.e., ~31 ppt Os, and ~22 ppt Ir; Peucker-Ehrenbrink and Jahn, 2001). Only two samples, 91R1_102–104.5 from the UIM, and 265R2_9–11 from the LIMB, show enrichments in Ir and Os concentrations by one order of magnitude, with 250 ppt Ir and 125 ppt Os, and 324 ppt Ir and 344 ppt Os, respectively. Additionally, the UIM sample 93R2_11–12.5 displays only an enrichment in Os, with 410 ppt, but a UCC-like Ir content of 22 ppt. Suevite samples are characterized by Os (27–134 ppt), and Ir (2–10 ppt) contents which are relatively similar to (for Os) and lower than (for Ir) those of impact melt rocks. The granite and amphibolite display Os contents of 22–26 ppt, comparable to the UCC composition. The Ir contents of granite range, between 1–8 ppt which is lower than the average UCC value of ~22 ppt (Peucker-Ehrenbrink and Jahn, 2001). The dacite has an Os concentration of 105 ppt, associated with an Ir content of 3 ppt. Given the higher uncertainty (see Section 5.4), some care should be taken with the samples

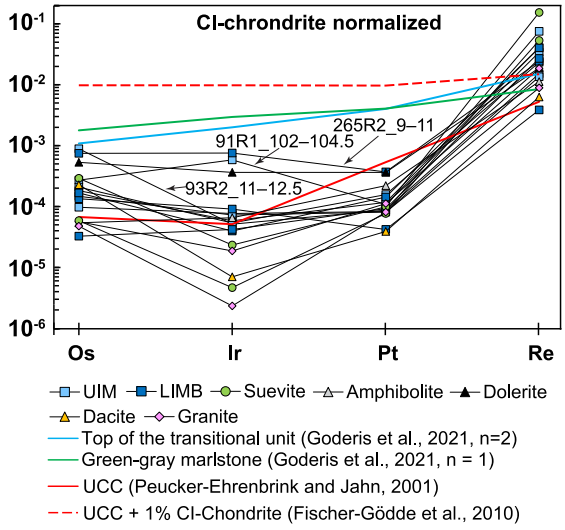

Fig. 6. CI-chondrite-normalized HSE abundance patterns, with normalization values from McDonough and Sun (1995). The impact melt samples generally display crustal HSE compositions with only three samples enriched in Os and/or Ir, which are still lower than those of the upper transitional unit and green-gray marlstone samples from the core section 40R1 (Goderis et al., 2021). Rhenium is generally enriched relative to both the upper continental crust and the transitional unit and was probably added following post-impact alteration from a long-lived hydrothermal system (Kring et al., 2020).

exhibiting very low Ir contents (<10 ppt). In contrast, the dolerite sample constitutes a more enriched lithology, with Os and Ir concentrations reaching 245 and 156 ppt, respectively. The dolerite Os and Ir composition reveals mantle-like affinity, plotting toward the primitive upper mantle (and chondritic) composition (Fig. 7), with a Os/Ir of 1.57, close to the primitive upper mantle value of 1.12 (Becker et al., 2006), and the chondritic Os/Ir of ~1.07 (Fischer-Gödde et al., 2010). Platinum concentrations for the UIM and LIMB samples range between 40 and 352 ppt, values which are below the average UCC Pt content of ~510 ppt (Peucker-Ehrenbrink and Jahn, 2001). Similarly to Ir and Os, only LIMB sample 265R2_9–11 is clearly enriched in Pt, at 352 ppt, while the second highest Pt content is two times lower, i.e., 149 ppt in UIM sample 93R1_21–23.5. In the case of the suevite samples, Pt contents are relatively similar to those of impact melt rocks with 73–94 ppt. Pre-impact lithologies display Pt concentrations of 77–106 ppt for granite and dacite, whereas amphibolite and dolerite show higher contents (i.e., 210 and 346 ppt, respectively). Finally, Re contents in impact melt rocks are more scattered relative to the other investigated HSEs, ranging from 145 to 2828 ppt. The Ir/Pt of the impact melt rocks varies from 0.13 to 2.43, higher than the UCC Ir/Pt of ~0.04 (Peucker-Ehrenbrink and Jahn, 2001), and encompassing the primitive upper mantle and CI-chondrite Ir/Pt ratio of ~0.45 and ~0.48, respectively (Becker et al., 2006; Fischer-Gödde et al., 2010). The Re contents are high (>1200 ppt) in UIM samples displaying the green phase (i.e., 88R3_45–47.5, 89R1_59–61.5, and 91R1_102–104.5), which are characterized by elevated CaO contents. Similar high Re contents are observed in the lower transitional unit, characterized also by very high CaO, i.e., generally more than 40 wt.% (Goderis et al., 2021). Suevites are characterized by elevated Re contents (2003–5800 ppt), while pre-impact lithologies display Re contents ranging from 237 to 710 ppt. Interelement plots between Os and Ir ($R^2 = 0.20$), and Ir and Pt ($R^2 = 0.53$) are shown on Fig. 7, demonstrating a relative decoupling between these elements, albeit less important in the case of Ir and Pt.

5.4. Re–Os isotope systematics

Measured $^{187}Os/^{188}Os$ ratios for 18 samples are given in Table 2 and range between 0.20 and 1.09, while Re–Os isotopic compositions are reported in Fig. 8. Measured $^{187}Os/^{188}Os$ ratios in the impact melt rocks display significant variations, ranging from an unradiogenic value of 0.1840 for the LIMB sample 265R2_9–11 to a more radiogenic value of 2.086 for the LIMB sample 303R3_22.5–25. A relatively good correlation ($R^2 = 0.80$) is noted between measured $^{187}Os/^{188}Os$ ratios and the Os concentrations in the impact melt rocks (Fig. 9b), with the more unradiogenic $^{187}Os/^{188}Os$ ratios in samples with the highest Os contents. The suevite samples have $^{187}Os/^{188}Os$ ratios of 0.6163 (for sample 41R1_106–108), and 1.1390 (for sample 58R3_8–10.5), broadly within the range of the impact melt rocks. Compared to impactite samples, the dolerite and the dacite samples show less radiogenic compositions, with $^{187}Os/^{188}Os$ ratios of 0.1700 and 0.2015, accompanied by

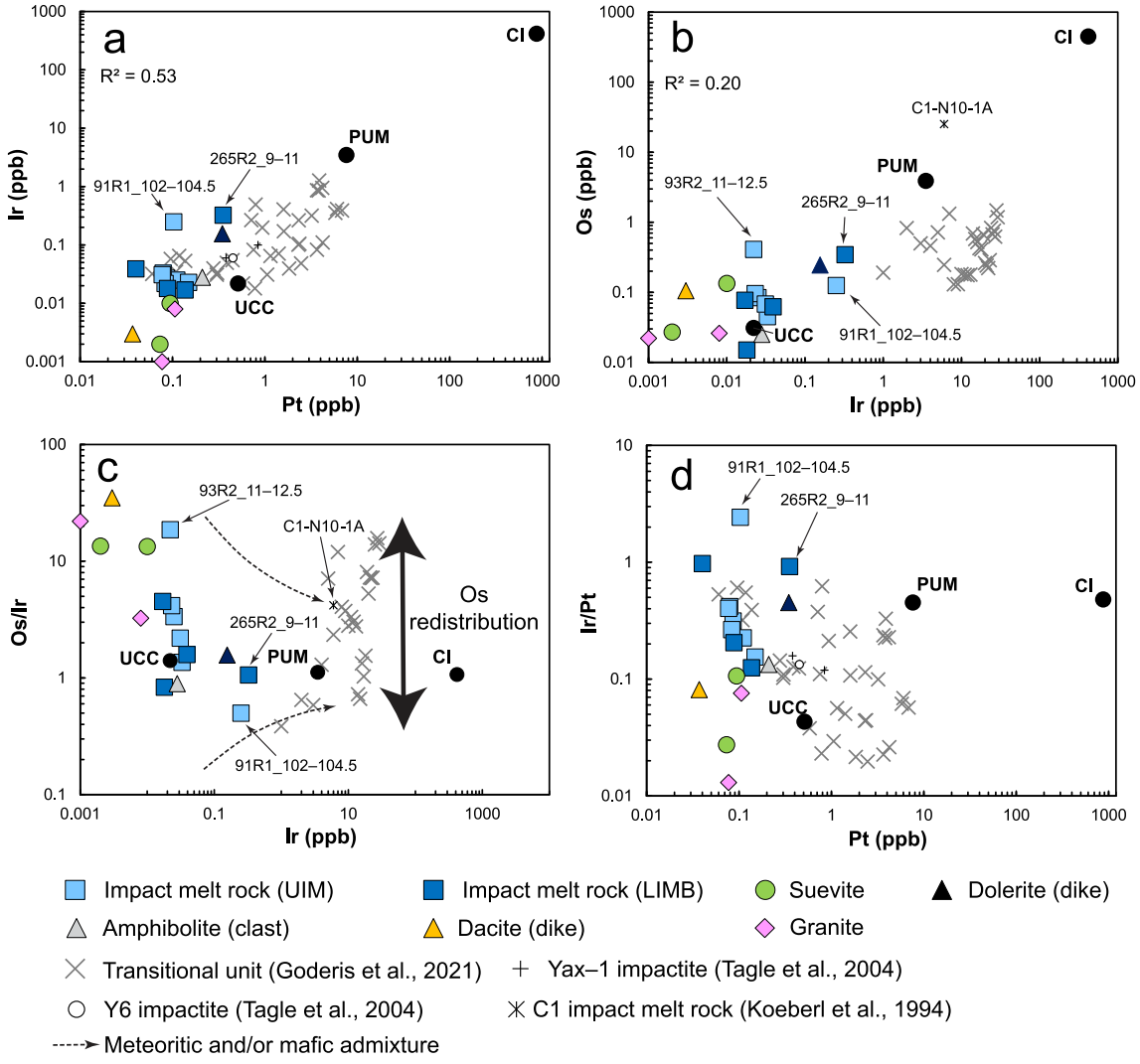

Fig. 7. Highly siderophile element compositions of the investigated samples, with average compositions of upper continental crust (UCC), primitive upper mantle (PUM), and CI-chondrites (CI) from Peucker-Ehrenbrink and Jahn (2001), Becker et al. (2006), and Fischer-Gödde et al. (2010), respectively. a–b) Bivariate diagrams of Ir versus Pt, and Os versus Ir. The impact melt samples generally display limited covariation. c) Os/Ir versus Ir diagram showing a slight trend towards PUM and CI composition for two impact melt samples, while transitional unit samples (Goderis et al., 2013) are clearly more enriched in Ir than the PUM composition, supporting the presence of meteoritic material within the transitional unit. d) Ir/Pt ratio versus Pt diagram, with impact melt samples plotting generally towards UCC compositions as no clear enrichment in Pt was observed.

relatively high Os contents of 245 and 105 ppt, respectively. While having relatively low Os contents, i.e., 22–26 ppt, the two granite samples are characterized by $^{187}Os/^{188}Os$ ratios, ranging from ~0.157 to ~0.161, well below the average UCC value of ~1.4 (Peucker-Ehrenbrink and Jahn, 2001). Finally, the amphibolite displays a more radiogenic composition than all the other samples, with a $^{187}Os/^{188}Os$ ratio of ~2.47, associated with a very low Os content of 25 ppt.

Measured $^{187}Os/^{188}Os$ ratios were back-calculated to 66.05 Ma (Table 2; Sprain et al., 2018). Recalculation to the time of impact is preferred here to know the Os isotopic composition at the time of formation of the impact melt rocks. Both measured and age-corrected $^{187}Os/^{188}Os$ ratios are similar, excepted for the amphibolite sample which has a measured $^{187}Os/^{188}Os$ ratio of ~2.47 and an age-corrected $^{187}Os/^{188}Os$ ratio of ~2.39. Therefore, the $^{187}Os/^{188}Os$ ratios provided in the text refer to measured values, the age-corrected values being stated in other cases.

The $^{187}Re/^{188}Os$ ratios of the impact melt rocks vary from as low as ~6.7 to as high as ~341, with the highest $^{187}Re/^{188}Os$ ratio (i.e., one UIM and two LIMB samples with $^{187}Re/^{188}Os$ higher than 100) observed in samples that have high $^{187}Os/^{188}Os$ ratios, i.e., above 1 (Fig. 8a). Elevated $^{187}Re/^{188}Os$ are reported for suevite samples with values of 201 for 41R1_106–108, and 350 for 58R3_8–10.5. Dolerite and dacite display lower $^{187}Re/^{188}Os$ ratios compared to the ones discussed above, with 13.5 and 10.6, respectively. The amphibolite and granite samples have $^{187}Re/^{188}Os$ ratios of 79.8 and 72.7–125, respectively. When plotting $^{187}Os/^{188}Os$ versus $^{187}Re/^{188}Os$ ratios for impact

melt rock samples, we obtain a so-called "errorchron" (see Fig. 8a), with a high scattering indicated by a mean square weighted deviation (MSWD) of 67, associated with an apparent age of 339 ± 113 Ma. This apparent age is similar, but with a higher uncertainty, as the U–Pb ages obtained on zircons from the granite, clustering around 334 ± 2.3 Ma (Ross et al., 2022).

6. DISCUSSION

6.1. Geochemistry of the impact melt rocks: mixing of felsic and mafic target lithologies

The major and trace element results (Tables S2 and S3), as well as petrographic observations for the investigated samples are in excellent agreement with previous work on impact melt rocks from the Chicxulub Expedition 364 drill core by de Graaff et al. (2022) and Schulte et al. (2021), which suggested that they formed by mixing and melting of granite and dolerite pre-impact basement rocks mainly, with (or without) incorporation of carbonate target rock material. While trace element compositions are relatively similar for both LIMB and UIM samples, with some variations only observed for specific trace elements (see Fig. S4), the major element contents of the two impact melt rocks units display more significant compositional variations. These are probably related to the heterogeneity of the impact melt, also in combination with a heterogeneous distribution of pre-impact lithology clasts at the hand sample scale (Morgan et al., 2017). Two mixing lines were calculated on a LOI-free basis for the CaO, MgO, Fe_2O_3, Al_2O_3, and TiO_2 contents (Fig. S3) between (1) dolerite and granite, representing the less evolved and the most evolved lithologies, as well as the most abundant pre-impact magmatic lithologies in the sample suite compared to the mafic amphibolite, which is far less abundant (found only as scarce, small centimeter-sized, clasts; see also, de Graaff et al., 2022), (2) average limestone composition (estimated by de Graaff et al., 2022) and granite to highlight the addition of carbonate material (or not) within the impact melt rocks. The LIMB samples plot relatively well along the mixing line between dolerite and granite for MgO, Fe_2O_3, and TiO_2, with a limited offset. In the case of CaO, LIMB samples show a clear offset, being depleted relative to the mixing line. They seem to follow a trend between the granite composition and the composition of LIMB sample 265R2_9–11, which is characterized by having a major and trace element composition similar to dolerite (i.e., a basaltic composition with low SiO_2 and high Fe_2O_3 and MgO contents). This genetic link is confirmed by μXRF mapping (Fig. S5) and petrographic investigations, which show that this sample is mainly a partially melted dolerite dike, with no contribution from a granitic component in the impact melt rock. Additionally, variations in the CaO content were observed between two dolerite dikes by de Graaff et al. (2022), with CaO contents ranging from as low as 2.40 wt.% to up to 10.7 wt.%. These variations in the CaO content in dolerite may be due to a variable abundance of post-impact calcite veins crosscutting the dolerite. Consequently, the LIMB probably results from the mixing between a granitic (felsic) and a dolerite (mafic) component characterized by low CaO contents (below 5 wt.%). In the case of the UIM (and suevite) samples, μXRF maps (Fig. S5) and petrographic observations have shown that carbonate material is mainly present as carbonate clasts and as sparry calcite within the green schlieren-textured matrix. These trends are also reflected in terms of whole-rock major element contents, with the UIM and suevite samples generally plotting in the area between the granite–dolerite and the granite–limestone mixing lines, and displaying enrichment in CaO and depletions in MgO, Fe_2O_3, and, to a lesser extent, TiO_2 contents (Fig. S3). The abundance of carbonate material within the UIM is even more significant in samples displaying the schlieren texture, or dominated by the green phase, i.e., located between 712.30 and 737.10 mbsf. These samples have an average CaO content of 11.2 wt.%, more than the double compared to the other UIM samples, with an average CaO content of 4.72 wt.%. The 80R2_126–128 sample, which is an impact melt rock clast within the suevite unit, shows a CaO content and an overall major element composition closer to the LIMB than to the UIM (i.e., having an evolved composition with 66.3 wt.% SiO_2, and plotting on or in proximity to the granite–dolerite mixing line), thus, this impact melt sample incorporated a relative limited amount of carbonate material. The carbonate component is even more abundant in the suevite samples, which have up to 28.6 wt.% CaO in the investigated samples (i.e., values up to 40.5 wt.% CaO were reported in the upper part of the suevite sequence by Kaskes et al., 2022). The Al_2O_3 contents for both LIMB and UIM are more scattered, probably an effect, as already noted in our petrographic observations and in previous works, of the presence of clay minerals (phyllosilicates) resulting from low-temperature alteration of (vitric) melt (see also, Kring et al., 2020; Simpson et al., 2020; Schulte et al., 2021; de Graaff et al., 2022). According to mixing calculation of de Graaff et al. (2022), most of the impact melt rock major element compositions may be explained by the mixing of ~30–60% of dolerite with the granite (see also Supplementary Material).

Regarding the trace element data, the CI-chondrite-normalized trace element abundance pattern of the LIMB sample 267R3_52.5–55.5 is highly similar to those of the granites, suggesting that this lithology dominates the composition of the whole sample (Fig. S4). This is further supported by petrographic observations, indicating a higher abundance of clasts and brecciated granitoid-derived material relative to the other LIMB samples investigated, and is also in agreement with the major element analysis, as this sample shows the most felsic composition of all LIMB samples. On the other hand, the dolerite affinity of LIMB sample 265R2_9–11 is also reflected in the trace element compositions with, similarly to dolerite, depletions in Rb, Ba, and Th (Fig. S4 and Table S3). These observations further highlight the heterogeneous nature of the impact melt rocks (i.e., both UIM and LIMB) and their incomplete mixing, as indicated by the flow textures and the presence of undigested clasts, in major element, and, to a lesser extent, trace element compositions.

Table 2
Moderately and highly siderophile element abundances and Re–Os isotopic compositions of impact melt rocks, suevites, and pre-impact lithologies. Cr and Co contents were obtained by INAA, while Ni contents were obtained using bulk XRF measurements. *Sample investigated for HSE-Os analysis.

Sample	Depth (mbsf)	Cr (ppm)	Co (ppm)	Ni (ppm)	Re (ppb)	Os (ppb)	Ir (ppb)	Pt (ppb)	$^{187}Os/^{188}Os$	2σ	$^{187}Re/^{188}Os$	2σ	$(^{187}Os/^{188}Os)_i$
Impact melt rocks (UIM)													
80R2_126–128	707.2	10.9	7.48	4.20	–	–	–	–	–	–	–	–	–
83R1_22–24.5*	712.3	72.2	12.8	27.2	0.387	–	0.027	0.086	–	–	–	–	–
88R1_12–14.5	722.7	58.8	18.5	32.2	–	–	–	–	–	–	–	–	–
88R3_45–47.5*	724.9	94.9	12.7	25.0	1.528	0.084	0.025	0.111	0.6374	0.0090	92.545	2.776	0.6374
89R1_59–61.5*	726.2	67.1	12.8	26.2	2.828	0.045	0.033	0.079	1.0900	0.0300	341.210	10.240	1.0900
91R1_102–104.5*	732.8	82.3	15.6	29.2	1.290	0.125	0.250	0.103	0.4154	0.0240	51.029	1.531	0.4154
91R2_89–91.5	733.8	62.7	11.9	21.4	–	–	–	–	–	–	–	–	–
92R2_89–91.5	737.1	52.3	12.8	25.5	–	–	–	–	–	–	–	–	–
92R3_39–41	737.8	69.6	15.6	26.2	–	–	–	–	–	–	–	–	–
93R1_21–23.5*	738.1	57.8	15.1	26.0	0.883	0.096	0.023	0.149	0.4363	0.0095	45.555	1.367	0.4363
93R1_121–123.5	739.1	58.1	13.7	29.0	–	–	–	–	–	–	–	–	–
93R2_11–12.5*	739.3	65.4	14.3	24.8	0.573	0.410	0.022	0.083	0.2025	0.0028	6.722	0.202	0.2025
95R1_18–20	744.1	55.3	12.5	22.5	–	–	–	–	–	–	–	–	–
95R1_84–87	744.8	57.6	11.1	15.7	–	–	–	–	–	–	–	–	–
95R2_45–47.5*	745.3	58.3	13.8	25.8	0.511	0.068	0.031	0.077	0.3189	0.0035	36.835	1.105	0.3189
Impact melt rocks (LIMB)													
202R2_48.5–53*	1026.3	155	25.2	83.7	0.145	0.062	0.039	0.040	0.2029	0.001	11.277	0.338	0.2029
265R2_9–11*	1216.5	299	58.2	180	0.915	0.344	0.324	0.352	0.1844	0.002	12.760	0.383	0.1844
267R3_52.5–55.5	1224.4	59.1	9.88	31.7	–	–	–	–	–	–	–	–	–
277R1_59.5–62	1253.0	31.8	17.8	22.5	–	–	–	–	–	–	–	–	–
277R1_88–92*	1253.3	41.7	20.0	26.0	1.524	0.077	0.017	0.136	1.0610	0.024	105.910	3.180	1.0610
277R2_25–27	1253.9	37.5	18.1	20.6	–	–	–	–	–	–	–	–	–
290R1_66–68	1292.0	39.2	14.0	20.2	–	–	–	–	–	–	–	–	–
292R2_66–68.5*	1299.4	53.9	18.1	23.7	–	0.075	–	–	0.5851	0.030	–	–	–
294R1_67.5–70	1304.4	17.0	7.76	3.50	–	–	–	–	–	–	–	–	–
303R3_22.5–25*	1334.4	45.0	17.8	19.2	1.014	0.015	0.018	0.088	2.0860	0.016	309.600	9.290	2.0860
Suevites													
41R1_106–108*	620.4	38.1	9.68	17.5	5.800	0.134	0.010	0.094	0.6163	0.0017	201.67	–	0.6163
58R3_8–10.5*	673.7	52.5	11.5	18.1	2.003	0.027	0.002	0.073	1.1390	0.0170	350.31	–	1.1390
Pre-impact lithologies													
80R2_61–63.5 (amphibolite)*	706.6	181	32.4	81.0	0.424	0.025	0.028	0.210	2.4740	–	79.790	–	2.3862
105R2_83–89 (felsite)	772.8	105	26.2	103	–	–	–	–	–	–	–	–	–
140R2_5–8 (dolerite)*	854.6	542	68.3	266	0.710	0.245	0.156	0.346	0.1700	0.0040	13.547	–	0.1700
238R1_101–103.5 (dacite)*	1135.1	13.7	8.22	9.60	0.237	0.105	0.003	0.037	0.2015	0.0069	10.600	–	0.2015
136R2_20–25 (granite)*	851.4	7.3	1.90	2.10	0.698	0.026	0.008	0.106	0.1569	0.0098	124.56	–	0.1569
200R3_12.5–15 (granite)*	1021.0	10.9	2.69	2.80	0.335	0.022	0.001	0.077	0.1609	0.0081	72.710	–	0.1609

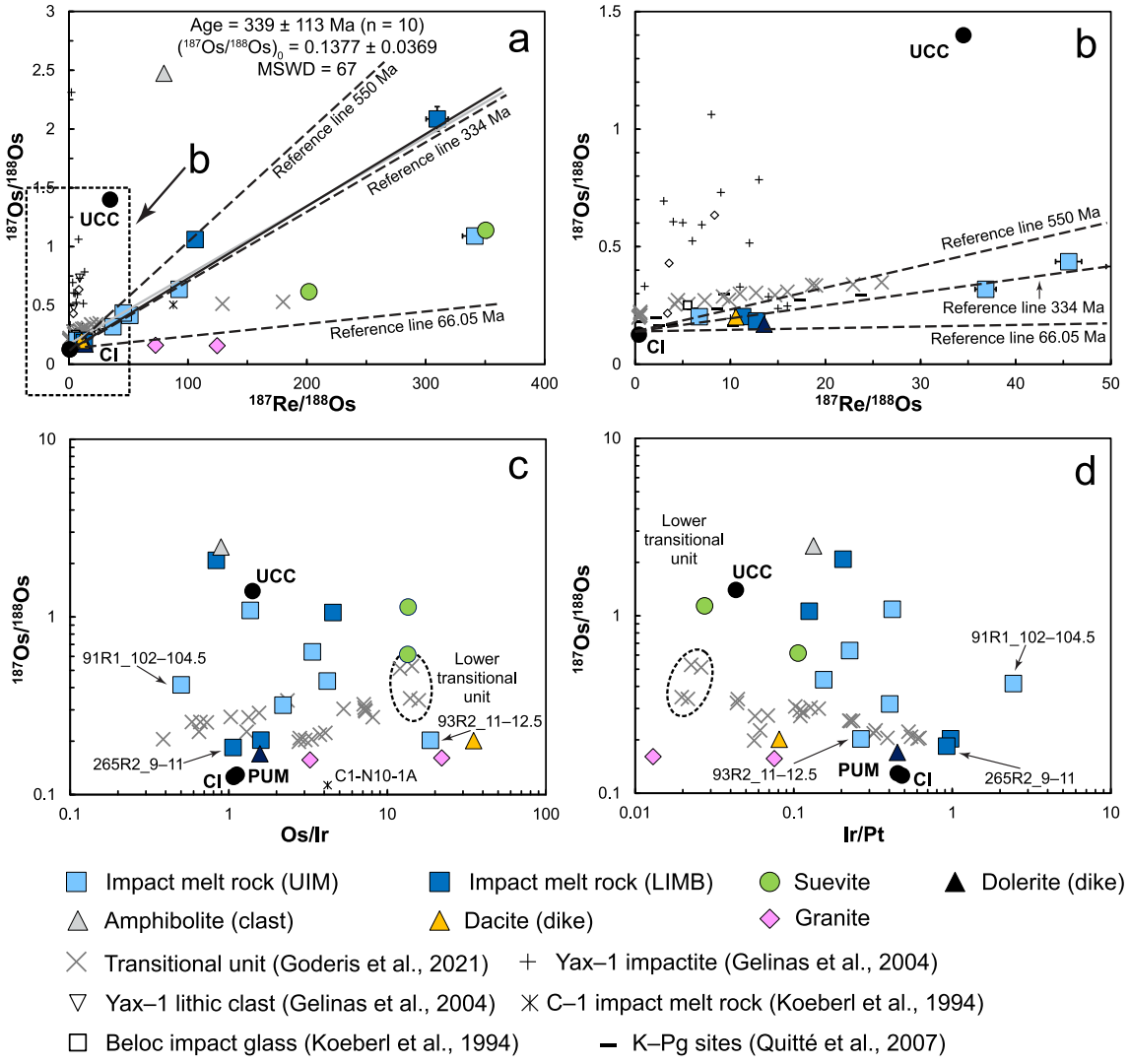

Fig. 8. a) Re–Os isotopic compositions of the investigated samples. An isochron was calculated, using IsoplotR (Vermeesch, 2018), for impact melt rocks (black line), giving an errorchron (high MSWD). The calculated apparent age and characteristics of the errorchron are given within the plot. The calculated uncertainty on the apparent age is two sigma with overdispersion. For comparison, a second isochron (gray line) is calculated for the transitional unit samples (Goderis et al., 2021). The transitional unit errorchron gives an apparent age of 333 ± 100 Ma, a $^{187}Os/^{188}Os_i$ of 0.20763, and a MSWD of 1200. Strong variations in the $^{187}Re/^{188}Os$ ratios are also observed. The dashed frame represents the Fig. 8b. b) Enlarged view of (a) with two isotopic trends that can be identified, i.e., the trend formed by the investigated samples, and similar to the Re–Os compositions in the transitional unit, K–Pg boundary sites, Beloc impact glass, and some Yax–1 samples, and a second trend formed by Yax–1 samples between chondritic and crustal compositions. In (a) and (b) two calculated reference lines for ~66.05 (age of the impact) and ~334 Ma (age of the granite) were added. A ~550 Ma (Pan-African) reference line was also added in (a). The Os isotopic signature of the granites plots towards the ~66.05 Ma reference line, which may indicate that the system was disrupted by the impact. c) Osmium isotopic composition versus Os/Ir ratio. UIM sample 93R2_11–12.5 has a composition similar to those of the lower transitional unit, characterized by a high abundance of sulfide minerals. d) Osmium isotopic composition versus Ir/Pt ratio. In contrast to Fig. 8c, sample 93R2_11–12.5 shows a composition closer to the mantel/chondritic compositions. The average values of upper continental crust (UCC), primitive upper mantle (PUM), and CI-chondrite (CI) are derived from Peucker-Ehrenbrink and Jahn (2001), Meisel et al. (2001), and Fischer-Gödde et al. (2010).

6.2. Search for the presence of an impactor component

There is no obvious correlation of Cr, Co, Ni, HSE abundances, and the Re–Os isotopic compositions with depth in the core (see Fig. 2), nor any specific enrichment in the abundances of these elements in a given unit or lithology. Only a decrease of the Re concentrations and the $^{187}Os/^{188}Os$ ratio is present in the UIM samples with increasing depth (from nearly crustal values to unradiogenic values; Fig. 2b), however, this is probably due to textural variations (i.e., with the green phase being absent in the lower part of the UIM) and further supports that the chemical and isotope variations observed are mainly related to the lithological nature of the samples, and/or to some

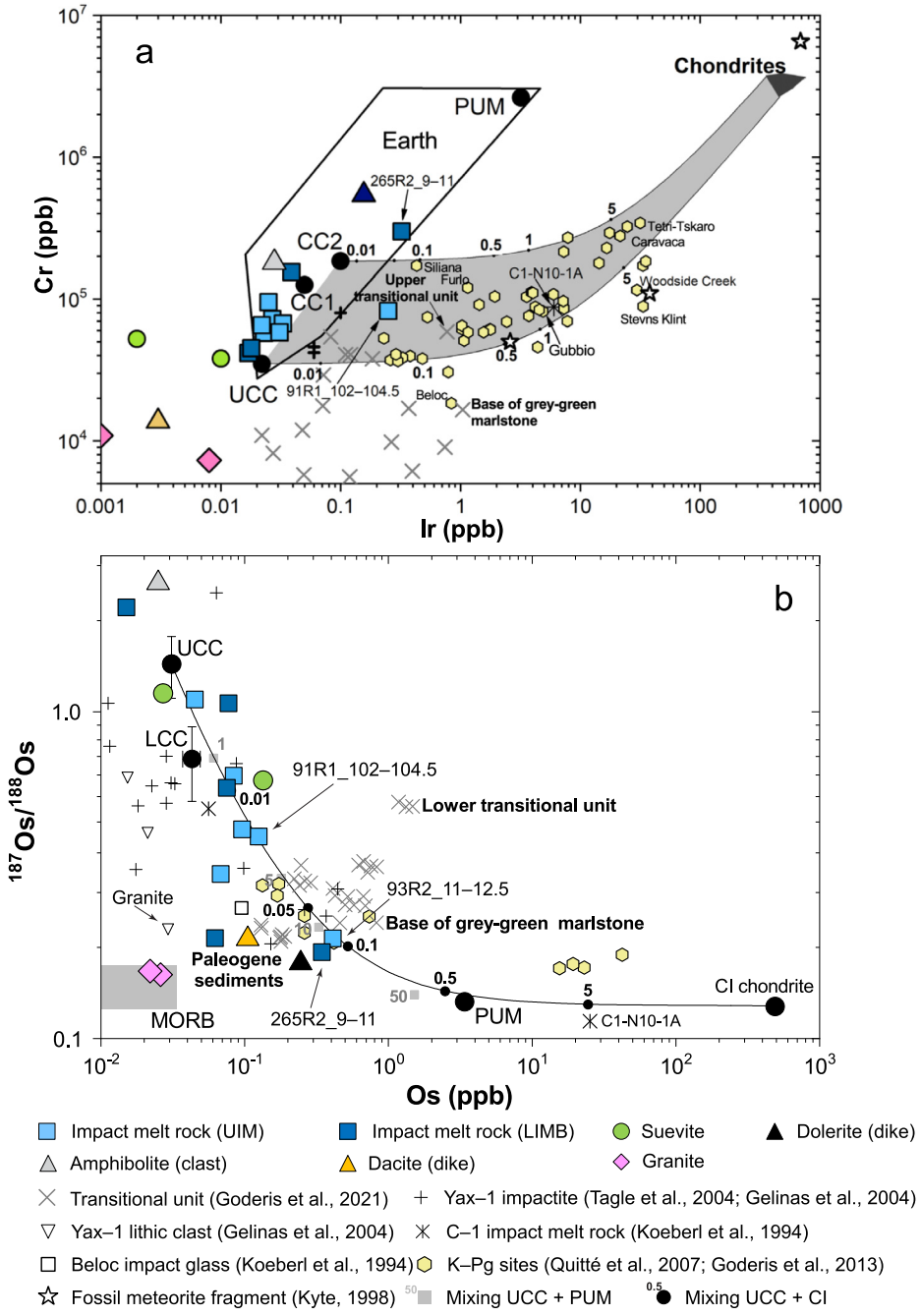

Fig. 9. a) Diagram of Cr versus Ir concentrations (modified from Tagle and Hecht, 2006; Goderis et al., 2021) presenting data from the investigated samples in this study, compared to the transitional unit samples, K–Pg boundary sites, Yax–1 impactites (Tagle et al., 2004), and a fossil meteorite fragment. The data are also compared with Cr and Ir compositions of various terrestrial lithologies and chondrites. The gray area displays the mixing trajectories between chondritic meteoritic material and crustal terrestrial target rocks. Earth field, upper continental crust (UCC), continental crust (CC), primitive upper mantle (PUM) compositions are from Tagle and Hecht (2006), and references therein. Suevites, granites and dacite are plotting well outside the typical terrestrial values with low Cr and Ir content. b) Osmium isotopic ratio versus Os concentration (based on Tagle and Hecht (2006), and references therein), with measured $^{187}Os/^{188}Os$ ratio versus Os concentration in the investigated samples, and compared with samples from the transitional unit (core section 40R1), impactites from Yax–1 (Gelinas et al., 2004), C1, Beloc impact glass, and other K–Pg boundary sites. Os isotopic composition of lithic clasts found in Yax–1 is also presented, especially the unradiogenic granite highlighted by an arrow. The curve represents a mixing line between upper continental crust (UCC) and CI-chondrite composition. The impact melt and suevite samples from drill core M0077A display relatively important variations in $^{187}Os/^{188}Os$ ratio, with several samples broadly following both the mixing curves between UCC and CI-chondrites, and UCC and primitive upper mantle (PUM), making the disentanglement between the mantle and meteoritic component impossible. The largest measured meteoritic contribution in the impact melt samples from the peak ring is between ~0.01 and 0.05%. With the two unradiogenic impact melt rocks more probably representing a mafic component or the effects of post-impact hydrothermal alteration. The measured granite samples display unusually unradiogenic $^{187}Os/^{188}Os$ ratios, plotting within the MORB field (Schiano et al., 1997).

heterogeneities within the impact melt rocks. Similarly, a decrease with increasing depth in the core is also observed for the CaO content of the UIM samples, probably indicating that the carbonate component is less abundant within the deepest part of the UIM unit. Thus, Re is expected to be enriched in Ca-rich lithologies, such as the green phase of the UIM, as well as suevite samples, according to their Re and CaO compositions.

In general, the moderately siderophile elements (Cr, Co, and Ni) compositions of the investigated impact melt rocks are relatively homogeneous, broadly comprised between the pre-impact lithology compositions, with no sample plotting close to the CI-chondrite component (Fig. 4). These trends in Cr, Co, and Ni are also visualized by μXRF mapping (Fig. 5b–d), showing low abundance values in the suevites, UIM, and dacite samples, in contrast to enriched values for the amphibolite, dolerite, and LIMB sample 265R2_16–19 (which is from the same LIMB dike as 265R2_9–11) and to a lesser degree sample 202R2_48.5–53. The main information given is the enrichment in Ni and Cr observed within the decomposed olivines, and the spinel-group minerals, respectively (see Fig. 5e–f), in dolerite samples. Indeed, previous observations on dolerite have shown the presence of numerous submicroscopic crystallites of Ni- and Co-bearing Fe-sulfides (containing up to ~10 wt.% Ni and ~1 wt.% Co) within the sheet silicate aggregates replacing olivine (see also de Graaff et al., 2022 and Supplementary Material). Applying μXRF mapping on all of the 17 samples at the same time has the benefit that it displays a high-resolution (sub-mm), semi-quantitative overview of the enrichments and depletions of selected elements in the different lithological and mineralogical phases (Kaskes et al., 2021).

When calculating mixing lines between the granite and the dolerite end-members in the case of Ni versus Cr, and Ni versus Co (Fig. 4a–b), both UIM and LIMB samples plot along this mixing line with no or only minor offsets along the granite–CI-chondrite mixing line. The moderately siderophile element compositions of the UIM and LIMB may be reproduced by the admixture of ~5–20%, and up to ~80% of dolerite component to the granite. In contrast, the "transitional unit" samples and K–Pg boundary clays (Goderis et al., 2013, and references therein; Goderis et al., 2021) show a clear enrichment in Ni (Fig. 4), which is characteristic of the incorporation of chondritic material (Tagle and Berlin, 2008). Therefore, the Cr, Co, and Ni contents in impact melt rocks from the Chicxulub peak ring are mostly derived from the mixing between the dolerite (specifically the incorporation of Ni, Cr, and Co carrier phases) and granite components. Importantly, these moderately siderophile elements grant further insight into target rock contributions to the impact melt rock but yield no distinct proof of meteoritic admixture.

The HSE abundance patterns of most of the impact melt rocks (Fig. 6) are typical for crustal composition, as shown by their low Os, Ir, and Pt contents, suggesting no or no significant admixture of a meteoritic component to these samples. The Os/Ir, Ir and Pt contents of impact melt rocks and suevites mostly spread between the pre-impact lithologies compositions. This suggests that the variation of Os/Ir, as well as the Ir and Pt contents in impact melt rocks and suevites seems mainly due to a mixing between these pre-impact components, and more specifically between granite and dolerite, without being affected by another external process. Additionally, nearly all the impact melt rock samples exhibit typical terrestrial Cr and Ir compositions (Fig. 9a), the exception being the Ir and, to a lesser extent, Cr concentrations of the suevite, dacite, and granite samples (i.e., lower than typical terrestrial values; Fig. 9a), confirming the low siderophile element content of some of the target lithologies, although an additional effect by hydrothermal alteration cannot be excluded.

Only three samples, two from the UIM (samples 91R1_102–104.5 and 93R2_11–12.5) and one from the LIMB (sample 265R2_9–11) show a clear enrichment in Os and/or in Ir relative to the average UCC composition (Fig. 6) and were thus considered as good candidates for potentially having incorporated a meteoritic component. However, the enrichment observed in these samples is below those recorded in the upper transitional unit and the green-gray marlstone in core 40R, in which an unambiguous meteoritic component was found (Goderis et al., 2021). Based on our petrographic investigations, as well as major and trace elements analysis, the impact melt rock sample 265R2_9–11 mainly consists of melted dolerite. Moreover, the Cr and Ir composition of this sample plots within terrestrial array (Fig. 9a), towards the primitive upper mantle, confirming the mantle-like (mafic) affinity of this specific impact melt rock sample. The HSE and Os isotopic compositions of sample 265R2_9–11 are also very similar to those measured in the dolerite sample (Table 2). Following these observations, the observed enrichment in HSE in this sample relative to the other impact melt samples (Fig. 6) is interpreted to be probably associated with the incorporation of dolerite, rather than a meteoritic admixture.

For the 93R2_11–12.5 UIM sample, only high Os was measured (410 ppt), whereas Ir content is low (22 ppt), resulting in a high Os/Ir ratio of 18.6. Similarly, high Os/Ir ratio (12.0–15.8), associated with high Ni, Os, Re, and Pt content, but low Ir contents, were measured in the lower part of the "transitional unit", more specifically in the section between 617.32 and 617.34 mbsf (Goderis et al., 2021). They were thought to be the result of hydrothermal remobilization of HSEs of crustal and possibly meteoritic origin, while Ir, being less mobile (Racki et al., 2011; Schmitz et al., 2011; Krull-Davatzes et al., 2012) compared to, e.g., Os, Re, and Pt, was not affected (Goderis et al., 2021). Unlike the samples from the "transitional unit", no distinct enrichment in Ni, Re, and Pt content is observed in our sample, suggesting that perhaps Os was remobilized. This sample also exhibits the second highest Cu content (49.3 ppm), compared to the average Cu content of ~27 ppm for the UIM samples (see Table S3). This suggests this sample experienced, to some extent, hydrothermal alteration with the formation of chalcopyrite, also observed commonly in impact melt rock by Kring et al. (2020). Therefore, the less radiogenic $^{187}Os/^{188}Os$ signature measured (0.2025) compared to other impact melt samples could either be due to a ~0.1% contribution of chondritic

material or a ~10% of a mantle component, with the latter being more probable as the Cr and Ir contents of this sample plot within the terrestrial field (Fig. 9a). Additionally, a Re-loss following post-impact hydrothermal alteration may also explain the low $^{187}Os/^{188}Os$ ratio measured in sample 93R2_11–12.5.

Finally, the UIM sample 91R1_102–104.5 displays enrichments in both Os and Ir relative to the UCC composition, i.e., 125 and 250 ppt, respectively, and plots toward the primitive upper mantle and CI-chondrite compositions in the Os/Ir ratio versus Ir content diagram (Fig. 7c). Importantly, no dolerite clasts were noticed during our petrographic investigations, and the major element composition is not mafic (i.e., 58.7 wt.% SiO_2). Based on the Cr versus Ir diagram, and the Os isotopic composition (Fig. 9), we estimate that the UIM sample 91R1_102–104.5 may contain a distinct but highly diluted meteoritic component, at most about 0.01 to 0.05%. However, the $^{187}Os/^{188}Os$ ratio of 0.4154, close to crustal values (Fig. 9b), does not unambiguously confirm that the HSE and Os isotopic compositions are of meteoritic origin. Sample 91R1_102–104.5 also has the highest As content of all UIM samples, of 10.8 ppm, three times more than the average of 3.7 ppm for the UIM samples (see Table S3). Arsenic is generally known to be an important constituent of geothermal fluids (Ballantyne and Moore, 1988). The Cu content of this sample is lower (15.6 ppm) than the UIM average, suggesting that post-impact hydrothermal fluid alteration implying sulfide minerals precipitation (Kring et al., 2020) probably did not affect significantly the HSE abundances and the Os isotopic composition. However, the mafic component present within the impact melt rocks could also explain the specific HSE content and Re–Os isotopic composition of this sample. In this case, it is difficult to unambiguously verify the presence of a small meteoritic component.

The majority of impact melt rocks and the suevites $^{187}Os/^{188}Os$ ratios broadly follow the mixing lines between (1) UCC and CI-chondrite and (2) UCC and primitive upper mantle, which also corresponds to a line between amphibolite and dolerite (and even dacite) compositions (Fig. 9b). Based on the major element data, mixing between dolerite and amphibolite cannot explain the andesitic composition of impact melt rocks. The dacite is also relatively rare, with only three dikes identified throughout the entire core (Morgan et al., 2017; de Graaff et al., 2022), and a significant contribution from this lithology to the Os isotopic composition seems unlikely.

The terrestrial Cr and Ir signature of the majority of the impact melt rocks suggests that the $^{187}Os/^{188}Os$ isotopic ratio variation likely represents mixing between a mantle-like component and a crustal component, although the granite (and dacite) samples display unusual, MORB-like $^{187}Os/^{188}Os$ ratios, coupled with very low Cr and Ir contents (see next section). Finally, both the amphibolite and LIMB sample 303R3_22.5–25 are characterized by supra-crustal $^{187}Os/^{188}Os$ isotopic ratios of 2.47 and 2.09, and low Os contents of 15 and 25 ppt, respectively. However, the $^{187}Re/^{188}Os$ ratio of the amphibolite is lower (~79.8) than that of sample 303R3_22.5–25 (~309), and these two samples do not seem to follow an isochron. As such, the high $^{187}Re/^{188}Os$ ratio measured in LIMB sample 303R3_22.5–25 suggests, more probably, a late addition of Re, perhaps from hydrothermal fluid origin. Therefore, the HSE contents and the Re–Os isotopic composition of the impact melt rocks and suevites indicate a highly heterogeneous distribution of both pre-impact material and the occurrence of a highly diluted possible meteoritic component in a single UIM sample.

This heterogeneity, associated with previous petrographic investigations, suggests that during its formation, the impact melt rock did not have sufficient time to fully homogenize and experienced a fast quenching, especially in the case of the UIM (see Schulte et al., 2021). The combined major element, moderately siderophile elements, and Ir–Pt data are consistent with mixing line between granite and dolerite. However, Re–Os isotopic data are inconsistent with such a mixture. This may suggest that the Os isotopic composition and HSE patterns within the impact melt rocks and suevites underwent modifications induced by the post-impact hydrothermal alteration (Simpson et al., 2020), remobilizing both Re and Os, that the granite samples represent outlier compositions, or that another currently unsampled component contributed to the impact melt. The siderophile elements, as well as Re–Os isotopic signatures of the granite may have been affected by pre-impact hydrothermal metasomatic event(s) that occurred approximately 50 Myr after granite formation (Feignon et al., 2021). The obtained data illustrate the challenges to characterize and unambiguously identify a distinct projectile contamination in the presence of a mafic component and/or with a hydrothermal overprint.

6.3. Alteration and hydrothermal overprint

Previous work and observations (Morgan et al., 2017; Kring et al., 2020) have indicated evidence for alteration and hydrothermal overprint throughout the entire drill core. The post-impact hydrothermal system was long lived, occurring for at least 1 Myr (Kring et al., 2020). This hydrothermal overprint is evidenced by the occurrence of secondary minerals, such as clay, chlorite, pyrite, etc., that were observed within the impactites (i.e., both impact melt rocks and suevites), as well as in the pre-impact material (Kring et al., 2020; Goderis et al., 2021). Following this evidence, in the presence of a high amount of sulfide minerals, chalcophile elements (Cu, Zn) may be redistributed and lead to local enrichments. Such enrichments in Cu and Zn, as well as Ni, are seen in the lower transitional unit (617.32 to 617.34 mbsf; Goderis et al., 2021). Indeed, not only chalcophile, but also siderophile elements may be redistributed and this could explain some of the features observed in some samples, like the low amount of Cr, Co, and Ni of the granites compared to the average UCC composition, and the fractionated Os/Ir and Ir/Pt ratios (Table 1, Figs. 4a–b, 6).

Rhenium, and, to a lesser extent, Os are also known to be highly mobile during alteration and weathering processes (Wallace et al., 1990; Jaffe et al., 2002; Wimpenny et al., 2007; Aiglsperger et al., 2021). The Re concentrations

of impact melt rocks and suevites are scattered, but in general higher than the average UCC Re content (Fig. 6), and even higher than the Re contents of the transitional unit (Goderis et al., 2021), suggesting a significant hydrothermal remobilization of Re within the suevites and impact melt rocks. This is further supported by the large number of samples displaying a very high $^{187}Re/^{188}Os$ ratio, plotting far to the right of the "errorchron" (Fig. 8). The "errorchron" given by the measured $^{187}Os/^{188}Os$ versus the $^{187}Re/^{188}Os$ ratios has significant scatter (Fig. 8a–b), with Re–Os isotopic compositions varying from unradiogenic, i.e., chondritic (and mantle-like) compositions to Re-rich compositions. However, none of the pre-impact lithologies have $^{187}Re/^{188}Os$ ratios higher than ~125, further supporting a probable late addition of Re, driven by the hydrothermal cell. Even if the apparent age shows a large uncertainty (339 ± 113 Ma), it is within the range of the granite age of ~334 ± 2.3 Ma obtained for zircons (Ross et al., 2022). Transitional unit samples (Goderis et al., 2021) also yield a relatively similar apparent age of ~333 ± 100 Ma (Fig. 9a), which may confirm that the granite represents the main felsic component for most impact melt rocks, and more generally, impactites of the Chicxulub peak ring. However, both measured $^{187}Os/^{188}Os$ ratios of granite samples plot along the 66.05 Ma (impact age) reference line, in contradiction with its estimated age. This possibly indicates that the Re–Os isotopic system was disturbed following the impact event.

The granite Re–Os isotopic signature is highly unusual, plotting in the MORB array (Fig. 9b), i.e., with low Os content (22–26 ppt), which are values relatively typical, albeit slightly lower than, upper crustal rocks (~31 ppt; Peucker-Ehrenbrink and Jahn, 2001), whereas the measured $^{187}Os/^{188}Os$ ratio is highly unradiogenic (0.16), and thus similar to mantle values (~0.13; Meisel et al., 2001). Additionally, the Ir contents (1–8 ppt) are below UCC composition (~22 ppt; Peucker-Ehrenbrink and Jahn, 2001). A similar unusually low $^{187}Os/^{188}Os$ ratio is observed for the dacite (0.20) associated with a low Ir content (3 ppt). The $^{187}Re/^{188}Os$ ratio of the granites are also relatively high, i.e., ~73 and ~124 (Fig. 8a), suggesting they may have been affected by the addition of Re following the hydrothermal overprint. In the case of the dacite, the $^{187}Re/^{188}Os$ ratio is relatively low (~11). Possibly, the Os was also remobilized by the long-lived post-impact hydrothermal system in the granite and dacite samples, as the granite plots close to the 66.05 Ma reference line on the Re–Os isotopic diagram (Fig. 8a). The remobilization may have been eased by the high porosity of the granites (10% on average; Christeson et al., 2018) which could have further enhanced fluid circulation. One granite clast investigated in Yax–1 drill core has a similar low Os concentration of ~29 ppt and is coupled with a relatively unradiogenic $^{187}Os/^{188}Os$ ratio of 0.2169 (see Fig. 9b; Gelinas et al., 2004). This may suggest that the unusual Re–Os isotopic signature of the investigated granites is not restricted to our samples from the Hole M0077A drill core, but could represent a common feature within the Chicxulub impact structure, highlighting the effects of post-impact hydrothermal alteration. However, no further investigations were made to assess the degree of alteration experienced by this granite in Yax–1. Thus, the unusual Os isotopic signature of the granites and dacite may be related to the hydrothermal overprint that affected this granite, rather than representing a primary magmatic, or source inherited signal. Further investigations on additional samples would be needed to confirm this trend.

6.4. Comparison with other Chicxulub drill cores

Our geochemical investigations of the HSE contents and Re–Os isotope systematics in impact melt rocks are compared with results obtained for the "transitional unit" of the Chicxulub peak ring (core 40R) presented by Goderis et al. (2021). Unlike the impact melt rocks from our study, the transitional unit displays unambiguous evidence for a meteoritic component admixture, with generally high Ni, Os, Ir, and Pt contents (see Figs. 4–6 and Table 1). Samples from the transitional unit show compositions more comparable to chondritic addition to the local background signature (Figs. 6–8), whereas the Ir/Pt and Os/Ir ratios show variations similar to those of the impact melt rocks from this study. The $^{187}Os/^{188}Os$ isotopic composition of the transitional unit is more homogeneous and covers a relatively narrow range (~0.21–0.35, excluding the lower transitional unit samples) compared to impact melt rocks and suevites from this study. Within the transitional unit, contamination by up to ~0.1% of meteoritic material was found (Goderis et al., 2021). This is nearly one order of magnitude higher compared to the hypothetic meteoritic contamination of up to ~0.01–0.05% recorded in UIM sample 91R1_102–104.5 (Fig. 9). This suggests a higher dilution and heterogeneous distribution of the meteoritic matter in the impact melt rock units, or that only the mafic component was present. On the other hand, the dolerite, representing the mafic component, appears to have contributed significantly to the HSE budget and to the Re–Os isotopic signature observed in some impact melt rock samples (e.g., sample 265R2_9–11).

The Cr, Co, Ni, and HSE concentrations of impact melt rocks and suevites are also similar to those previously measured in impactites recovered in other drill cores, i.e., C1, Y6, and Yax–1 (Koeberl et al., 1994; Tuchscherer et al., 2004a; Tagle et al., 2004; Gelinas et al., 2004). Comparable variations in the $^{187}Os/^{188}Os$ ratio, from radiogenic crustal to unradiogenic (i.e., chondritic) values, were measured in previous drill cores (Table 1; see also Koeberl et al., 1994; Gelinas et al., 2004). The meteoritic component is difficult to discern, and compositions are broadly within the range of those of the UCC, and, when identified, the admixture of meteoritic material to the impactites is not higher than ~0.1%. The Cr versus Ir compositions of impactites from the Yax–1 and Y6 drill cores (Fig. 9a) measured by Tagle et al. (2004) are close to the overlapping area between the continental crust–chondrites mixing area and the Earth field shown in Fig. 9a, and thus might indicate a barely resolvable meteoritic component. Additionally, the Yax–1 impactites have relatively mafic to intermediate compositions (44.2–55.8 wt.% SiO_2), and thus, may also reflect a possible contribution of a mafic component, excluding

impactites displaying a significant (>10 wt.% CaO) carbonate component (Tagle et al., 2004; Tuchscherer et al., 2004a). This poses further implications regarding the origin of the HSE and Re–Os compositions of the impactite samples from Yax–1, as even if a minor heterogeneous meteoritic component may be present, the contribution from a mafic lithology cannot be excluded or disentangled. Additionally, Tuchscherer et al. (2004a) explained the composition of Yax–1 impactites, especially in the green impact melt breccia (unit 4, 861–884 meters depth), by the presence of a significant mafic component. Mafic clasts were identified in impact-melt bearing polymict impact breccias from Yax–1, e.g., gabbro and amphibolite, but no dolerite (samples YAX-1_836.34 and Yax-1_832.83; Kring, 2005, and references therein; Schmieder et al., 2017). Amphibolite was also identified as a clast in the Y6 core (sample Y6 N14 p4c; Kettrup and Deutsch, 2003). The only exception where a significant impactor component was identified in Chicxulub drill core material was in the case of powdered splits of impact melt rock from the C1 (C1-N10-1A, 1393–1394 meters below sea level) and Y6 (Y6-N19, 1377–1379.5 meters below sea level) drill cores (Sharpton et al., 1992; Koeberl et al., 1994; Schuraytz et al., 1996). These samples display high Ir and Os concentrations, up to ~15 ppb and ~25 ppb, respectively, associated with a chondritic $^{187}Os/^{188}Os$ ratio, corresponding to a contribution of chondritic material of up to ~5% (Fig. 9b). However, their interpretation remains difficult due to their stratigraphic position and may represent atypical sample heterogeneity, as the HSEs in these samples do not show chondritic elemental abundance ratios and may represent a mafic component that was not sampled (Sharpton et al., 1992; Koeberl et al., 1994; Schuraytz et al., 1996). Additionally, subsequent investigations of sample Y6-N19 revealed significant hydrothermal alteration (e.g., anhydrite veining, zeolites, and secondary calcite) and did not find such high Ir contents (<0.01 ppb; Kring and Boynton, 1992; Tagle et al., 2004, and references therein).

When adding available $^{187}Os/^{188}Os$ and $^{187}Re/^{188}Os$ isotope data from previous work (see Table 1), the Re–Os isotopic signatures recorded in the transitional unit, Yax–1 and C1 drill cores, and in K–Pg sites around the globe (Koeberl et al., 1994; Gelinas et al., 2004; Quitté et al., 2007; Goderis et al., 2021) follow broadly the same trend as the studied impact melt rocks, but show generally lower $^{187}Re/^{188}Os$ ratio (<30) towards chondritic/mantle-like compositions, with only two transitional unit samples having a $^{187}Re/^{188}Os$ ratio higher than 100. These two latter samples are from the bottom of the transitional unit (617.34 mbsf) where a strong hydrothermal signature in HSE pattern and pyrite chemistry is identified (Goderis et al., 2021), and thus, support a late addition of Re, explaining these high $^{187}Re/^{188}Os$ ratios. Therefore, the impact melt, suevite, and even granite samples displaying $^{187}Re/^{188}Os$ higher than 100 represent compositions in accordance with a post impact hydrothermal overprint which caused an addition of Re after remobilization of this element. Regarding the Yax–1 impactites (Gelinas et al., 2004), while some of these follow the same trend as the previously described samples, a second trend, albeit somewhat scattered towards the average UCC, as well as the amphibolite sample, for the Re–Os isotopic composition can be identified and may represent a different crustal component, or a larger proportion of amphibolite, that could have been incorporated within Yax–1 impactites but not in C-1 or in the M0077A drill core, or even in the K–Pg boundary sites. A contribution of the amphibolite, albeit small, may also explain the difference observed between the calculated initial transitional unit (0.2076) and the impact melt rock (0.1377) $^{187}Os/^{188}Os$ ratios (Fig. 8a). This second trend does not follow the calculated ~66.05, ~334 Ma, and ~550 Ma (Pan-African) reference lines in Fig. 8a–b. Thus, even a more pronounced addition of Pan-African material, thought to be an important component of the Yucatán peninsula basement rocks (Zhao et al., 2020; Feignon et al., 2021, and references therein), does not explain the Re–Os isotopic composition of these Yax–1 impactites.

Therefore, the common features of the impact melt rocks, and more broadly, impactites recovered in drill cores within the Chicxulub impact structure (including the Hole M0077A core) are, on the one hand their relatively similar Ni, Cr, Co, and HSE compositions, and, on the other hand the strong heterogeneity of HSE distribution from a sample to another, at a relatively small scale (Koeberl et al., 1994; Tagle et al., 2004; Tuchscherer et al., 2004a; Goderis et al., 2021). Generally, the incorporation of meteoritic material is low (up to ~0.1% in rare samples; Gelinas et al., 2004; Goderis et al., 2021), compared to the more distal K–Pg boundary layers displaying contributions of meteoritic material of up to ~5%, and to the upper transitional unit topping the peak ring, recording unambiguously the admixture of chondritic material (see Fig. 9; Quitté et al., 2007; Goderis et al., 2013; Goderis et al., 2021). Moreover, the heterogeneous distribution of meteoritic material within the impact melt rocks seems to be a common feature of the Chicxulub impact structure, and not only restricted to the peak ring. The absence of a high amount of projectile component within the impact melt rocks (and more generally all impactites) of the Chicxulub structure may be due to the role played by the nature of the interface between the target rock and the impactor in the admixture process, as suggested by Tagle et al. (2004). In the case of Chicxulub, the crystalline basement was covered with volatile-rich layers, i.e., ~3-km-thick carbonate platform, anhydrite, and seawater (Lopez Ramos, 1975; Kring, 2005), which may have prevented the mixing process between the meteoritic material and the target rock (Tagle et al., 2004).

6.5. Lack of ubiquitous impactor signal explained

No distinct HSE composition from dolerite and other pre-impact lithologies was measured in the investigated Chicxulub peak ring impact melt rock samples, which does not allow to unambiguously distinguish between a mafic and a meteoritic contribution to the impact melt rocks. Previous work on Chicxulub impactites from within the impact structure (Koeberl et al., 1994; Gelinas et al., 2004; Tagle et al., 2004; Tuchscherer et al., 2004a) indicates that probably only a minor meteoritic material was incorporated (and heterogeneously) in the impactites. Interestingly, a

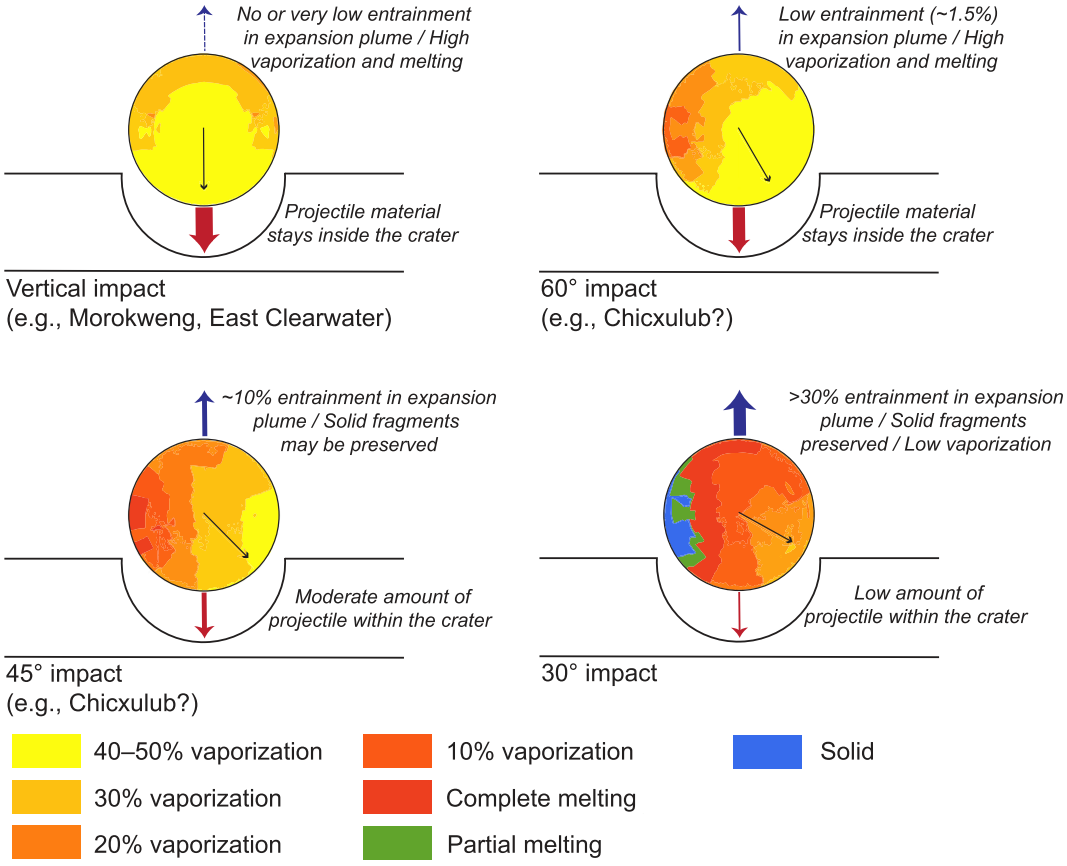

Fig. 10. Diagram modified from Pierazzo and Melosh (2000), showing the distribution of vaporization and melting inside a 10-km diameter projectile according to the impact angle relative to the target surface. In the case of vertical and steeply-inclined (60°) impact, significant vaporization and melting occur, with the meteoritic material being mainly concentrated at the bottom of the crater. The proportion of projectile material ejected and entrained within the expansion plume increases with decreasing angle (percentages provided are given at t = 3 s after the impact; Pierazzo and Melosh, 1999).

possible explanation for this low incorporation of the projectile could be the impact angle, as numerical modeling suggests that the Chicxulub impact structure formed, most probably, following an oblique impact, with an angle between 45 and 60° to the horizontal (Collins et al., 2020). This is an important aspect to consider because the impact angle has an effect on the amount of projectile vaporization, which decreases with the impact angle (Pierazzo and Melosh, 2000). For vertical and steeply-inclined (60°) impacts, at least ~30% of the impactor mass is vaporized, the remaining part being generally completely melted (see Fig. 11 of Pierazzo and Melosh, 2000). Below 60°, parts of the projectile may survive as solid fragments (from the trailing half of the projectile, subject to lesser shock pressures), with the vaporization becoming nearly non-existent for very shallow impact angles (~15°). For the assumed 45–60° impact angle of the Chicxulub impact event, a substantial proportion of the impactor material was likely vaporized (~10–30%, see Fig. 10) and melted (Pierazzo and Melosh, 1999, 2000), and deposited outside the impact crater, as indicated by the marine Os isotopic composition record and Ir concentrations (Paquay et al., 2008).

The preservation within the K–Pg boundary ejecta of a significant meteoritic component (e.g., Quitté et al., 2007; Goderis et al., 2013), and of a small, 2.5 mm, (fossil) meteorite fragment (Kyte, 1998), is consistent with the scenario of an oblique impact event, probably below 60°, where parts of the impactor survived as solid phase and/or melted material, according to hydrocode modeling (Pierazzo and Melosh, 1999, 2000). For 45 and 60° impact angles, ~10% and ~1.5% of the projectile is entrained within the expansion plume, respectively (Fig. 10; Pierazzo and Melosh, 1999). However, as the numerical simulation ends only 3 seconds after the impact, it is possible that these percentages represent minimal estimates, as the expansion plume should develop over a longer duration (Pierazzo and Melosh, 1999). Hydrocode modeling has shown, especially for steeply-inclined impact (60°), that the projectile material stays mainly inside the crater, and moves downward (Pierazzo and Melosh, 2000). Therefore, in this case, the preserved meteoritic material may be located in the deepest impact melt rock units (up to ~3 km depth, Morgan et al., 2016) of the Chicxulub impact structure, rather than in the shallowest impact melt rocks investigated here. Unfortunately, these deep impact melt rocks were not yet recovered by any of the available drill cores.

An impact angle closer to 45° would be more consistent in order to explain the observed distribution of meteoritic matter, which is concentrated mainly in the K–Pg impact

ejecta, and also the preservation of a solid meteorite fragment in sediments retrieved from a K–Pg boundary in the North Pacific Ocean (Kyte, 1998), which seems unlikely at higher impact angles (Fig. 10). The vaporization and ejection of the meteoritic matter may have prevented its incorporation at high amounts within the impact structure, and may explain the generally low (<0.1%) meteoritic contamination measured in the Chicxulub impactites. The sheer volume of impact melt rocks produced at Chicxulub, may have enhanced the dilution of impactor component (see also Grieve and Cintala, 1992), and could also explain this low, or not detectable, meteoritic contribution.

6.6. Implications for projectile material identification and distribution in large impact structures

Similarly low levels of meteoritic material in the impactites was found in several impact structures around the world (e.g., Bosumtwi, Manicouagan, Lake Saint Martin, Ries), suggesting possibly similar mechanisms of formation of the impactites (Tagle et al., 2004, and references therein). On a broader perspective, similar impact processes, e.g., an oblique impact event, may be involved to explain the lack of a detectable meteoritic component within the aforementioned impact structures (Pierazzo and Melosh, 2000). Difficulties with unambiguously identifying a meteoritic signature in impact melt rocks using the HSEs budget and Re–Os isotopic system were also encountered in impact structures characterized by target lithologies that contain a large mafic component and/or that were affected by hydrothermal alteration. The Lonar crater, located in India, formed in mafic (i.e., basalt) target rock (Schulz et al., 2016). Lonar crater basalts have relatively unradiogenic $^{187}Os/^{188}Os$ ratios, but still higher than the Chicxulub peak ring dolerite (~0.35, and two radiogenic basalts with $^{187}Os/^{188}Os$ ratios above 1.5; Schulz et al., 2016). Some impactites at Lonar crater have significantly higher HSE abundances relative to basalt, as well as distinct Re–Os isotopic ratios, which allows for the identification of a meteoritic contribution of ~0.02% (Schulz et al., 2016). However, results of Cr isotopic studies suggest significant incorporation of chondritic material, i.e., between ~1–3% (Mougel et al., 2019). Impact spherules have been found to contain even larger contributions, i.e., up to 8% (Das Gupta et al., 2017). Another example is the Bosumtwi impact structure in Ghana, where the target rock has unusually high HSE contents, and thus, it was not possible to identify, and to quantify an unequivocal impactor contribution distinct from the crustal contribution in impactite samples recovered within the crater or in the proximal ejecta deposits (see also Goderis et al., 2007; McDonald et al., 2007). However, Koeberl and Shirey (1993) have shown (using Re and Os concentrations and Os isotopic compositions) that about 0.6% of a meteoritic component is incorporated in Ivory Coast tektites (i.e., distal ejecta from the Bosumtwi crater).

While at several large impact structures, such as Chicxulub, no or only minimal projectile contamination was detected in impactites from within the crater and/or in proximal ejecta deposits, there are other cases where a significant amount of meteoritic component was identified within the impact structure. An homogeneous chondritic contribution of ~2–5%, as well as a preserved meteorite fragment were identified within the impact melt rocks from the Morokweng impact structure (Koeberl et al., 1997; Koeberl and Reimold, 2003; Maier et al., 2006). Similarly, the investigated impact melt rocks from the ~22-km diameter East Clearwater Lake impact structure revealed the presence of ~8% of CI chondrite material (Grieve et al., 1980). In these two cases, the scenario of a vertical, or nearly vertical impact event relative to the target surface, where most of the projectile material stays within the crater (Fig. 10; Pierazzo and Melosh, 2000) are favored. The preservation of a meteorite fragment within the Morokweng impact melt rocks may also be explained by a relatively low impact velocity, with possibly a lower degree of vaporization and melting of the projectile (Maier et al., 2006). In the case of the East Clearwater Lake impact structure, it is suggested that peak shock pressures in the order of ~300 GPa were sufficient to vaporize the silicate component, but only melt the metal fraction of the projectile (Grieve et al., 1980). Therefore, the investigation of HSE abundances and Re–Os isotopic signatures of the impact melt rocks and ejecta deposits of large impact structures may provide useful information on the processes involved in the distribution of the impactor material.

7. CONCLUSIONS

As shown using major and trace element whole-rock concentrations, μXRF mapping, petrographic investigations, and consistent with previous works, the impact melt rocks in the Chicxulub peak ring mainly reflect mixing between a felsic and a mafic target lithology component (i.e., granite and dolerite). In the upper impact melt unit (UIM), carbonate material was also incorporated both within the green schlieren phase, and as clasts within the silicate black impact melt. Other pre-impact lithologies, such as dacite, amphibolite, and felsite, appear not to have contributed to the impact melt rock significantly.

While previous work at K–Pg boundary sites around the world, and also to some extent within the Chicxulub impact structure, has identified the presence of meteoritic matter, the impact melt rocks within the peak ring structure have a more complex geochemical signature. Most notably, the post-impact hydrothermal overprint as well as the mafic target rock contribution have affected the HSE compositions and the Re–Os isotopic signature significantly. The main mafic lithology in the Hole M0077A core is dolerite (with an accumulation of Ni and Co in pseudomorphosed olivine, and of Cr in spinel-group minerals), which shows a mantle-like signature with enrichments in the HSEs, and low $^{187}Os/^{188}Os$ ratio comparable to chondritic values, preventing an unambiguous identification of a contamination by the projectile). The effects of post-impact hydrothermal alteration also play an important role in remobilizing elements such as Ni, Re (especially with a late addition of Re, increasing the measured $^{187}Re/^{188}Os$ ratios of suevites, some impact melt rocks, and, to a lesser extent, granites), and Os either by fluid circulation or accumulation of HSEs

in sulfide phases (Goderis et al., 2021). Consequently, contributions of mafic material and hydrothermal overprint seem to be the most likely explanations for the observed HSE and Re–Os isotopic compositions within the Chicxulub peak ring impact melt rock. Nonetheless a potential meteoritic component in the impact melt cannot be fully excluded either, as a single UIM sample (91R1_102–104.5) indicates a possible projectile contribution of ~0.01–0.05%, nearly an order of magnitude lower than that recorded in the transitional unit, and in the Yax–1 drill core.

To summarize, at least five processes led to the currently observed impact melt rock moderately siderophile element, HSE, and Re–Os isotopic compositions: (1) enhanced excavation, vaporization of the impactor following a steeply inclined (possibly ~45°) impact, preventing and/or limiting the incorporation of meteoritic material (ejection within the expansion plume) within the impact melt rocks, (2) melting and mixing of a mafic (potentially dolerite) and a felsic (likely granite) component, with the incorporation of variable contributions of carbonate, and (3) the addition of a minor meteoritic component, (4) fast quenching (Schulte et al., 2021) leading to a heterogeneous chemical composition and distribution of the HSE–Os isotopic composition, and (5) remobilization of some moderately and HSEs such as Ni, Re, and Os following the onset of a long-living, post-impact hydrothermal system, further modifying the HSE budget. The variations in moderately siderophile element, HSE, and Re–Os isotopic compositions, reflect large heterogeneity within the impact melt, similar to what has been observed in previous works on impact melt rocks from different drill cores within the Chicxulub impact structure. This suggests that during its formation, the impact melt did not have sufficient time to fully homogenize, both physically and chemically, and that this process seems to be common to the entire Chicxulub impact structure and not restricted to the peak ring. The Chicxulub peak ring impact melt rocks represent an important example of the challenges associated with the unambiguous identification of a meteoritic component within terrestrial impact structures.

Declaration of Competing Interest

The authors declare that they have no known competing financial interests or personal relationships that could have appeared to influence the work reported in this paper.

ACKNOWLEDGEMENTS

This paper is dedicated to the memory of Günter W. Lugmair (1940–2021), for his pioneering work on isotopic analysis of the K–Pg boundary and in cosmochemistry in general. The Chicxulub drilling was funded by the IODP as Expedition 364, with co-funding from ICDP. Expedition 364 was implemented by ECORD, with contributions and logistical support from the Yucatán state government and Universidad Nacional Autónoma de México. Partial funding was provided by the University of Vienna doctoral school IK-1045 (P.I.: C.K.). We thank Peter Nagl and Marianne Schwarzinger for XRF sample preparation and analysis, and Dieter Mader for INAA and data processing. The AMGC team is supported by Research Foundation Flanders (FWO-Vlaanderen; project G0A6517N) and BELSPO (project Chicxulub); P.K. is an FWO PhD fellow (project 11E6619N; 11E6621N). S.G. and P.C. thank the EoS project "ET--HoME" for support and the VUB Strategic Research Program. P.C. thanks the FWO -- Hercules Program for financing the μXRF instrument at the VUB. This is contribution 70 of the DFG-funded ICPMS facilities at the Steinmann-Institute, University of Bonn. We thank Martin Schmieder and an anonymous reviewer for detailed and constructive reviews, as well as Marc Norman for editorial handling.

APPENDIX A. SUPPLEMENTARY MATERIAL

Supplementary data to this article can be found online at https://doi.org/10.1016/j.gca.2022.02.006.

REFERENCES

Aiglsperger T., González-Jiménez J. M., Proenza J. A., Galí S., Longo F., Griffin W. L. and O'Reilly S. Y. (2021) Open System Re-Os Isotope Behavior in Platinum-Group Minerals during Laterization? *Minerals* **11**, 1083.

Alvarez L. W., Alvarez W., Asaro F. and Michel H. V. (1980) Extraterrestrial cause for the Cretaceous-Tertiary extinction. *Science* **208**, 1095–1108.

Ballantyne J. M. and Moore J. N. (1988) Arsenic geochemistry in geothermal systems. *Geochim. Cosmochim. Acta* **52**, 475–483.

Becker H., Horan M. F., Walker R. J., Gao S., Lorand J.-P. and Rudnick R. L. (2006) Highly siderophile element composition of the Earth's primitive upper mantle: Constraints from new data on peridotite massifs and xenoliths. *Geochim. Cosmochim. Acta* **70**, 4528–4550.

Belza J., Goderis S., Keppens E., Vanhaecke F. and Claeys P. (2012) An emplacement mechanism for the mega-block zone within the Chicxulub crater, (Yucatán, Mexico) based on chemostratigraphy. *Meteorit. Planet. Sci.* **47**, 400–413.

Birck J. L., Barman M. R. and Capmas F. (1997) Re-Os isotopic measurements at the femtomole level in natural samples. *Geost. Newslett.* **21**, 19–27.

Brandon A. D., Humayun M., Puchtel I. S., Leya I. and Zolensky M. (2005) Geochemistry: Osmium isotope evidence for an s-process carrier in primitive chondrites. *Science* **309**, 1233–1236.

Chiarenza A. A., Farnsworth A., Mannion P. D., Lunt D. J., Valdes P. J., Morgan J. V. and Allison P. A. (2020) Asteroid impact, not volcanism, caused the end-Cretaceous dinosaur extinction. *Proc. Natl. Acad. Sci.* **117**, 17084–17093.

Christeson G. L., Gulick S. P. S., Morgan J. V., Gebhardt C., Kring D. A., Le Ber E., Lofi J., Nixon C., Poelchau M., Rae A. S. P., Rebolledo-Vieyra M., Riller U., Schmitt D. R., Wittmann A., Bralower T. J., Chenot E., Claeys P., Cockell C. S., Coolen M. J. L., Ferrière L., Green S., Goto K., Jones H., Lowery C. M., Mellett C., Ocampo-Torres R., Perez-Cruz L., Pickersgill A. E., Rasmussen C., Sato H., Smit J., Tikoo S. M., Tomioka N., Urrutia-Fucugauchi J., Whalen M. T., Xiao L. and Yamaguchi K. E. (2018) Extraordinary rocks from the peak ring of the Chicxulub impact crater: P-wave velocity, density, and porosity measurements from IODP/ICDP Expedition 364. *Earth Planet. Sci. Lett.* **495**, 1–11.

Claeys P., Kiessling W. and Alvarez W. (2002) Distribution of Chicxulub ejecta at the Cretaceous–Tertiary boundary. In *Catastrophic events and mass extinctions: impacts and beyond* (eds. C. Koeberl and K. G. MacLeod). Geological Society of America Special Paper 356, Boulder, Colorado, pp. 55–68.

Claeys P., Heuschkel S., Lounejeva-Baturina E., Sanchez-Rubio G. and Stöffler D. (2003) The suevite of drill hole Yucatàn 6 in the Chicxulub impact crater. *Meteorit. Planet. Sci.* **38**, 1299–1317.

Cohen A. S. and Waters F. G. (1996) Separation of osmium from geological materials by solvent extraction for analysis by thermal ionization mass spectrometry. *Anal. Chim. Acta* **332**, 269–275.

Collins G. S., Patel N., Davison T. M., Rae A. S. P., Morgan J. V., Gulick S. P. S. and IODP-ICDP Expedition 364 Science Party and Third-Party Scientists (2020) A steeply-inclined trajectory for the Chicxulub impact. *Nat. Commun.* **11**, 1480.

Creaser R. A., Papanastassiou D. A. and Wasserburg G. J. (1991) Negative thermal ion mass-spectrometry of osmium, rhenium and iridium. *Geochim. Cosmochim. Acta* **55**, 397–401.

Das Gupta R., Banerjee A., Goderis S., Claeys P., Vanhaecke F. and Chakrabarti R. (2017) Evidence for a chondritic impactor, evaporation-condensation effects and melting of the Precambrian basement beneath the 'target' Deccan basalts at Lonar crater, India. *Geochim. Cosmochim. Acta* **215**, 51–75.

de Graaff S. J., Kaskes P., Déhais T., Goderis S., Debaille V., Ross C. H., Gulick S. P. S., Feignon J.-G., Ferrière L., Koeberl C., Smit J., Matielli N. and Claeys P. (2022) New insights into the formation and emplacement of impact melt rocks within the Chicxulub impact structure, following the 2016 IODP-ICDP Expedition 364. *Geol. Soc. Am. Bull.* **134**, 293–315.

de Winter N. J. and Claeys P. (2017) Micro X-ray fluorescence (μXRF) line scanning on Cretaceous rudist bivalves: A new method for reproducible trace element profiles in bivalve Calcite. *Sedimentology* **64**, 231–251.

DePalma R. A., Smit J., Burnham D. A., Kuiper K., Manning P. L., Oleinik A., Larson P., Maurrasse F. J., Vellekoop J., Richards M. A. and Gurche L. (2019) A seismically induced onshore surge deposit at the KPg boundary, North Dakota. *Proc. Natl. Acad. Sci.* **116**, 8190–8199.

Feignon J.-G., Ferrière L., Leroux H. and Koeberl C. (2020) Characterization of shocked quartz grains from Chicxulub peak ring granites and shock pressure estimates. *Meteorit. Planet. Sci.* **55**, 2206–2223.

Feignon J.-G., de Graaff S. J., Ferrière L., Kaskes P., Déhais T., Goderis S., Claeys P. and Koeberl C. (2021) Chicxulub impact structure, IODP-ICDP Expedition 364 drill core: Geochemistry of the granite basement. *Meteorit. Planet. Sci.* **56**, 1243–1273.

Fischer-Gödde M., Becker H. and Wombacher F. (2010) Rhodium, gold and other highly siderophile element abundances in chondritic meteorites. *Geochim. Cosmochim. Acta* **74**, 356–379.

French B. M., Orth C. J. and Quintana C. R. (1989) Iridium in the Vredefort bronzite granophyre: Impact melting and limits on a possible extraterrestrial component. In *Proceedings, 19th Lunar and Planetary Science Conference*. Cambridge University Press, Cambridge/Houston, TX, Lunar and Planetary Institute, pp. 733–744.

Gelinas A., Kring D. A., Zurcher L., Urrutia-Fucugauchi J., Morton O. and Walker R. J. (2004) Osmium isotope constraints on the proportion of bolide component in Chicxulub impact melt rocks. *Meteorit. Planet. Sci.* **39**, 1003–1008.

Goderis S., Tagle R., Schmitt R. T., Erzinger J. and Claeys P. h. (2007) Platinum group elements provide no indication of a meteoritic component in ICDP cores from the Bosumtwi crater, Ghana. *Meteorit. Planet. Sci.* **42**, 731–741.

Goderis S., Tagle R., Belza J., Smit J., Montanari A., Vanhaecke F., Erzinger J. and Claeys P. (2013) Reevaluation of siderophile element abundances and across the Cretaceous-Paleogene (K–Pg) boundary: Implications for the nature of the projectile. *Geochim. Cosmochim. Acta* **120**, 417–446.

Goderis S., Sato H., Ferrière L., Schmitz B., Burney D., Kaskes P., Vellekoop J., Wittmann A., Schulz T., Chernonozhkin S. M., Claeys P., de Graaff S. J., Déhais T., de Winter N. J., Elfman M., Feignon J.-G., Ishikawa A., Koeberl C., Kristiansson P., Neal C. R., Owens J. D., Schmieder M., Sinnesael M., Vanhaecke F., Van Malderen S. J. M., Bralower T. J., Gulick S. P. S., Kring D. A., Lowery C. M., Morgan J. V., Smit J., Whalen M. T. and IODP-ICDP Expedition 364 Scientists (2021) Globally distributed iridium layer preserved within the Chicxulub impact structure. *Sci. Adv.* **7**, eabe3647.

Grieve R. A. F. and Cintala M. J. (1992) An analysis of differential impact melt-crater scaling and implications for the terrestrial impact record. *Meteoritics* **27**, 526–538.

Grieve R. A. F., Palme H. and Plant A. G. (1980) Siderophile-rich particles in the melt rocks at the E. Clearwater impact structure, Quebec: their characteristics and relationship to the impacting body. *Contrib. Mineral. Petrol.* **75**, 187–198.

Gulick S. P. S., Christeson G. L., Barton P. J., Grieve R. A. F., Morgan J. V. and Urrutia-Fucugauchi J. (2013) Geophysical characterization of the Chicxulub impact crater. *Rev. Geophys.* **51**, 31–52.

Gulick S. P. S., Bralower T. J., Ormö J., Hall B., Grice K., Schaefer B., Lyons S., Freeman K. H., Morgan J. V., Artemieva N., Kaskes P., de Graaff S. J., Whalen M. T., Collins G. S., Tikoo S. M., Verhagen C., Christeson G. L., Claeys P., Coolen M. J. L., Goderis S., Goto K., Grieve R. A. F., McCall N., Osinski G. R., Rae A. S. P., Riller U., Smit J., Vajda V., Wittmann A. and the Expedition 364 Scientists, (2019) The first day of the Cenozoic. *Proc. Natl. Acad. Sci. USA* **116**, 19342–19351.

Hildebrand A. R., Penfield G. T., Kring D. A., Pilkington M., Camargo Z. A., Jacobsen S. B. and Boynton W. V. (1991) Chicxulub crater: A possible Cretaceous/Tertiary boundary impact crater on the Yucatán Peninsula, Mexico. *Geology* **19**, 867–871.

Horan M. F., Walker R. J., Morgan J. W., Grossman J. N. and Rubin A. E. (2003) Highly siderophile elements in chondrites. *Chem. Geol.* **196**, 27–42.

Jaffe L. A., Peucker-Ehrenbrink B. and Petsch S. T. (2002) Mobility of rhenium, platinum group elements and organic carbon during black shale weathering. *Earth Planet. Sci. Lett.* **198**, 339–353.

Kaskes P., Déhais T., de Graaff S. J., Goderis S. and Claeys P. (2021) Micro–X-ray fluorescence (μXRF) analysis of proximal impactites: High-resolution element mapping, digital image analysis, and quantifications. In *Large Meteorite Impacts and Planetary Evolution VI: Geological Society of America Special Paper 550* (eds. W. U. Reimold and C. Koeberl). Geological Society of America Special Paper 550, Boulder, Colorado, pp. 171–206.

Kaskes P., de Graaff S. J., Feignon J.-G., Déhais T., Goderis S., Ferrière L., Koeberl C., Smit J., Wittmann A., Gulick S., Debaille V., Matielli N. and Claeys P. (2022) Formation of the Crater Suevite Sequence from the Chicxulub Peak Ring: a Petrographic, Geochemical, and Sedimentological Characterization. *Geol. Soc. Am. Bull.* **134**, 895–927.

Kettrup B. and Deutsch A. (2003) Geochemical variability of the Yucatàn basement: Constraints from crystalline clasts in Chicxulub impactites. *Meteorit. Planet. Sci.* **38**, 1079–1092.

Koeberl C. (1993a) Chicxulub Crater, Yucatan: Tektites, impact glasses, and the geochemistry of target rocks and breccias. *Geology* **21**, 211–214.

Koeberl C. (1993b) Instrumental neutron activation analysis of geochemical and cosmochemical samples: a fast and reliable method for small sample analysis. *J. Radioanal. Nucl. Chem.* **168**, 47–60.

Koeberl C. (1998) Identification of meteoritical components in impactites. In *Meteorites: Flux with Time and Impact Effects* (eds. M. M. Grady, R. Hutchison, G. J. H. McCall and D. A. Rothery). Geological Society Special Publication 140, London, United Kingdom, pp. 133–152.

Koeberl C. (2014) The Geochemistry and Cosmochemistry of Impacts. In *Treatise on Geochemistry (Second Edition)*, Volume 2 (eds. H. D. Holland and K. K. Turekian). Elsevier, Amsterdam, Netherlands, pp. 73–118.

Koeberl C. and Reimold W. U. (2003) Geochemistry and petrography of impact breccias and target rocks from the 145 Ma Morokweng impact structure, South Africa. *Geochim. Cosmochim. Acta* **67**, 1837–1862.

Koeberl C. and Shirey S. B. (1993) Detection of a Meteoritic Component in Ivory Coast Tektites with Rhenium-Osmium Isotopes. *Science* **261**, 595–598.

Koeberl C. and Sigurdsson H. (1992) Geochemistry of impact glasses from the K/T boundary in Haiti: Relation to smectites and a new type of glass. *Geochim. Cosmochim. Acta* **56**, 2113–2129.

Koeberl C., Sharpton V. L., Schuraytz B. C., Shirey S. B., Blum J. D. and Marin L. E. (1994) Evidence for a meteoritic component in impact melt rock from the Chicxulub structure. *Geochim. Cosmochim. Acta* **58**, 1679–1684.

Koeberl C., Reimold W. U. and Shirey S. B. (1996) Re–Os isotope and geochemical study of the Vredefort Granophyre: Clues to the origin of the Vredefort structure, South Africa. *Geology* **24**, 913–916.

Koeberl C., Armstrong R. A. and Reimold W. U. (1997) Morokweng, South Africa: A large impact structure of Jurassic-Cretaceous boundary age. *Geology* **25**, 731–734.

Koeberl C., Claeys P., Hecht L. and McDonald I. (2012) Geochemistry of impactites. *Elements* **8**, 37–42.

Kring D. A. (2005) Hypervelocity collisions into continental crust composed of sediments and an underlying crystalline basement: Comparing the Ries (~24 km) and Chicxulub (~180 km) impact craters. *Geochemistry* **65**, 1–46.

Kring D. A. and Boynton W. V. (1992) Petrogenesis of an augite-bearing melt rock in the Chicxulub structure and its relationship to K/T impact spherules in Haiti. *Nature* **358**, 141–144.

Kring D. A., Tikoo S. M., Schmieder M., Riller U., Rebolledo-Vieyra M., Simpson S. L., Osinski G. R., Gattacceca J., Wittmann A., Verhagen C. M., Cockell C. S., Coolen M. J. L., Longstaffe F. J., Gulick S. P. S., Morgan J. V., Bralower T. J., Chenot E., Christeson G. L., Claeys P., Ferrière L., Gebhardt C., Goto K., Green S. L., Jones H., Lofi J., Lowery C. M., Ocampo-Torres R., Perez-Cruz L., Pickersgill A. E., Poelchau M. H., Rae A. S. P., Rasmussen C., Sato H., Smit J., Tomioka N., Urrutia-Fucugauchi J., Whalen M. T., Xiao L. and Yamaguchi K. E. (2020) Probing the hydrothermal system of the Chicxulub impact crater. *Sci. Adv.* **6**, eaaz3053.

Krull-Davatzes A. E., Lowe D. R. and Byerly G. R. (2012) Mineralogy and diagenesis of 3.24 Ga meteorite impact spherules. *Precambrian Res.* **196–197**, 128–148.

Kyte F. T. (1998) A meteorite from the Cretaceous/Tertiary boundary. *Nature* **396**, 237–239.

Lambert P. (1982) Anomalies within the system: Rochechouart target rock meteorite. In *Geological Implications of Impacts of Large Asteroids and Comets on Earth*. Geological Society of America Special Paper 190, Boulder, Colorado, pp. 57–68.

Lopez Ramos E. (1975) Geological Summary of the Yucatan Peninsula. In *The Gulf of Mexico and the Caribbean* (eds. A. E. M. Nairn and F. G. Stehli). Springer, Boston, MA, pp. 257–282.

Lowery C. M., Bralower T. J., Owens J. D., Rodríguez-Tovar F. J., Jones H., Smit J., Whalen M. T., Claeys P., Farley K., Gulick S. P. S., Morgan J. V., Green S., Chenot E., Christeson G. L., Cockell C. S., Coolen M. J. L., Ferrière L., Gebhardt C., Goto K., Kring D. A., Lofi J., Ocampo-Torres R., Perez-Cruz L., Pickersgill A. E., Poelchau M. H., Rae A. S. P., Rasmussen C., Rebolledo-Vieyra M., Riller U., Sato H., Tikoo S. M., Tomioka N., Urrutia-Fucugauchi J., Vellekoop J., Wittmann A., Xiao L., Yamaguchi K. E. and Zylberman W. (2018) Rapid recovery of life at ground zero of the end-Cretaceous mass extinction. *Nature* **558**, 288–291.

Lubetskaya T. and Korenaga J. (2007) Chemical composition of Earth's primitive mantle and its variance: 1. Method and results. *J. Geophys. Res.* **112**, B03211.

Luguet A., Nowell G. M. and Pearson D. G. (2008) $^{184}Os/^{188}Os$ and $^{186}Os/^{188}Os$ measurements by negative thermal ionization mass spectrometry (N-TIMS): effects on interfering element and mass fractionation corrections on data accuracy and precision. *Chem. Geol.* **248**, 342–362.

Luguet A., Behrens M., Pearson D. G., Koenig S. and Herwartz D. (2015) Significance of the whole rock Re-Os ages in cryptically and modally metasomatized cratonic peridotites – Constraints from the HSE-Se-Te systematics. *Geochim. Cosmochim. Acta* **164**, 441–463.

Mader D. and Koeberl C. (2009) Using Instrumental Neutron Activation Analysis for geochemical analyses of terrestrial impact structures: Current analytical procedures at the University of Vienna Geochemistry Activation Analysis Laboratory. *Appl. Radiat. Isot.* **67**, 2100–2103.

Maier W. D., Andreoli M. A., McDonald I., Higgins M. D., Boyce A. J., Shukolyukov A., Lugmair G. W., Ashwal L. D., Gräser P., Ripley E. M. and Hart R. J. (2006) Discovery of a 25-cm asteroid clast in the giant Morokweng impact crater, South Africa. *Nature* **441**, 203–206.

McDonald I., Peucker-Ehrenbrink B., Coney L., Ferrière L., Reimold W. U. and Koeberl C. (2007) Search for a meteoritic component in drill cores from the Bosumtwi impact structure, Ghana: Platinum group element contents and osmium isotopic characteristics. *Meteorit. Planet. Sci.* **42**, 743–753.

McDonough W. F. and Sun S. (1995) The composition of the Earth. *Chem. Geol.* **120**, 223–253.

Meisel T., Walker R. J., Irving A. J. and Lorand J.-P. (2001) Osmium isotopic compositions of mantle xenoliths: a global perspective. *Geochim. Cosmochim. Acta* **65**, 1311–1323.

Meisel T., Reisberg L., Moser J., Carignan J., Melcher F. and Brügmann G. (2003) Re–Os systematics of UB-N, a serpentinized peridotite reference material. *Chem. Geol.* **201**, 161–179.

Morgan J. V., Gulick S. P. S., Bralower T., Chenot E., Christeson G., Claeys P., Cockell C., Collins G. S., Coolen M. J. L., Ferrière L., Gebhardt C., Goto K., Jones H., Kring D. A., Le Ber E., Lofi J., Long X., Lowery C., Mellett C., Ocampo-Torres R., Osinski G. R., Perez-Cruz L., Pickersgill A., Pölchau M., Rae A., Rasmussen C., Rebolledo-Vieyra M., Riller U., Sato H., Schmitt D. R., Smit J., Tikoo S., Tomioka N., Urrutia-Fucugauchi J., Whalen M., Wittmann A., Yamaguchi K. E. and Zylberman W. (2016) The formation of peak rings in large impact craters. *Science* **354**, 878–882.

Morgan J., Gulick S., Mellet C. L. and Green S. L. (2017) Chicxulub: Drilling the K-Pg impact crater. In *and the Expedition 364 Scientists*. International Ocean Discovery Program, College Station, Texas, p. 164 p..

Morgan J. W., Janssens M.-J., Hertogen J., Gros J. and Takahashi H. (1979) Ries impact crater, southern Germany: search for meteoritic material. *Geochim. Cosmochim. Acta* **43**, 803–815.

Mougel B., Moynier F., Koeberl C., Wielandt D. and Bizzarro M. (2019) Identification of a meteoritic component using chromium isotopic composition of impact rocks from the Lonar impact structure, India. *Meteorit. Planet. Sci.* **54**, 2592–2599.

Palme H., Janssens M. J., Takahashi H., Anders E. and Hertogen J. (1978) Meteoritic material at five large impact craters. *Geochim. Cosmochim. Acta* **42**, 313–323.

Paquay F. S., Ravizza G. E., Dalai T. K. and Peucker-Ehrenbrink B. (2008) Determining chondritic impactor size from the marine osmium isotope record. *Science* **320**, 214–218.

Pearson D. G. and Woodland S. J. (2000) Solvent extraction/anion exchange separation and determination of PGEs (Os, Ir, Pt, Pd, Ru) and Re-Os isotopes in geological samples by isotope dilution ICP-MS. *Chem. Geol.* **165**, 87–107.

Peucker-Ehrenbrink B. and Jahn B.-M. (2001) Rhenium-osmium isotope systematics and platinum group element concentrations: Loess and the upper continental crust. *Geochem. Geophys. Geosyst.* **2**, 1061.

Pierazzo E. and Melosh H. J. (1999) Hydrocode modeling of Chicxulub as an oblique impact event. *Earth Planet. Sci. Lett.* **165**, 163–176.

Pierazzo E. and Melosh H. J. (2000) Hydrocode modeling of oblique impacts: The fate of the projectile. *Meteorit. Planet. Sci.* **35**, 117–130.

Potts P. J. and Meisel T. (2015) Certificate of Analysis, IAG OKUM (Ultramafic rock). International Association of Geoanalysts. Available online at http://www.iageo.com.

Quitté G., Levasseur S., Capmas F., Rocchia R., Birck J. L. and Allègre C. J. (2007) Osmium, tungsten, and chromium isotopes in sediments and in Ni-rich spinel at the K-T boundary: signature of a chondritic impactor. *Meteorit. Planet. Sci.* **42**, 1567–1580.

Racki G., Machalski M., Koeberl C. and Harasimiuk M. (2011) The weathering-modified iridium record of a new Cretaceous-Palaeogene site at Lechówka near Chelm, SE Poland, and its palaeobiologic implications. *Acta Palaeontol. Pol.* **56**, 205–215.

Riller U., Poelchau M. H., Rae A. S. P., Schulte F. M., Collins G. S., Melosh H. J., Grieve R. A. F., Morgan J. V., Gulick S. P. S., Lofi J., Diaw A., McCall N., Kring D. A. and IODP-ICDP Expedition 364 Science Party (2018) Rock fluidization during peak-ring formation of large impact structures. *Nature* **562**, 511–518.

Ross C. H., Stockli D. F., Rasmussen C., Gulick S. P. S., de Graaff S. J., Claeys P., Zhao J., Xiao L., Pickersgill A. E., Schmieder M., Kring D. A., Wittmann A. and Morgan J. V. (2022) Evidence of Carboniferous arc magmatism preserved in the Chicxulub impact structure. *Geol. Soc. Am. Bull.* **134**, 241–260.

Rudnick R. L. and Gao S. (2014) Composition of the Continental Crust. In *Treatise on Geochemistry (Second Edition)*, Volume 4 (eds. H. D. Holland and K. K. Turekian). Elsevier, Amsterdam, Netherlands, pp. 1–51.

Sanford J. C., Snedden J. W. and Gulick S. P. S. (2016) The Cretaceous-Paleogene boundary deposit in the Gulf of Mexico: Large-scale oceanic basin response to the Chicxulub impact. *J. Geophys. Res. Solid Earth* **121**, 1240–1261.

Schiano P., Birck J.-L. and Allègre C. J. (1997) Osmium-strontium-neodymium-lead isotopic covariations in mid-ocean ridge basalt glasses and the heterogeneity of the upper mantle. *Earth Planet. Sci. Lett.* **150**, 363–379.

Schmieder M., Shaulis B. J., Lapen T. J. and Kring D. A. (2017) U-Th-Pb systematics in zircon and apatite from the Chicxulub impact crater, Yucatán, Mexico. *Geol. Mag.* **155**, 1330–1350.

Schmitz B., Heck P. R., Alwmark C., Kita N. T., Meier M. M. M., Peucker-Ehrenbrink B., Ushikubo T. and Valley J. W. (2011) Determining the impactor of the Ordovician Lockne crater: oxygen and neon isotopes in chromite versus sedimentary PGE signatures. *Earth Planet. Sci. Lett.* **306**, 149–155.

Schulte F. M., Wittmann A., Jung S., Morgan J. V., Gulick S. P. S., Kring D. A., Grieve R. A. F., Osinski G. R., Riller U. and IODP-ICDP Expedition 364 Science Party (2021) Ocean resurge-induced impact melt dynamics on the peak-ring of the Chicxulub impact structure, Mexico. *Int. J. Earth Sci.* **110**, 2619–2636.

Schulte P., Alegret L., Arenillas I., Arz J. A., Barton P. J., Bown P. R., Bralower T. J., Christeson G. L., Claeys P., Cockell C. S., Collins G. S., Deutsch A., Goldin T. J., Goto K., Grajales-Nishimura J. M., Grieve R. A. F., Gulick S. P. S., Johnson K. R., Kiessling W., Koeberl C., Kring D. A., MacLeod K. G., Matsui T., Melosh J., Montanari A., Morgan J. V., Neal C. R., Nichols D. J., Norris R. D., Pierazzo E., Ravizza G., Rebolledo-Vieyra M., Reimold W. U., Robin E., Salge T., Speijer R. P., Sweet A. R., Urrutia-Fucugauchi J., Vajda V., Whalen M. T. and Willumsen P. S. (2010) The Chicxulub asteroid impact and mass extinction at the Cretaceous-Paleogene boundary. *Science* **327**, 1214–1218.

Schulz T., Luguet A., Wegner W., van Acken D. and Koeberl C. (2016) Target rocks, impact glasses, and melt rocks from the Lonar crater, India: Highly siderophile element systematics and Sr-Nd-Os isotopic signatures. *Meteorit. Planet. Sci.* **51**(7), 1323–1339.

Schuraytz B. C., Sharpton V. L. and Marín L. E. (1994) Petrology of impact-melt rocks at the Chicxulub multiring basin, Yucatán, Mexico. *Geology* **22**, 868–872.

Schuraytz B. C., Lindstrom D. J., Marín L. E., Martinez R. R., Mittlefehldt D. W., Sharpton V. L. and Wentworth S. J. (1996) Iridium metal in Chicxulub impact melt: forensic chemistry on the K-T smoking gun. *Science* **271**, 1573–1576.

Sharpton V. L., Dalrymple G. B., Marin L. E., Ryder G., Schuraytz B. C. and Urrutia-Fucugauchi J. (1992) New links between the Chicxulub impact structure and the Cretaceous/Tertiary boundary. *Nature* **359**, 819–821.

Sharpton V. L., Lee S., Ryder G. and Schuraytz B. C. (1996) A model of the Chicxulub impact basin based on evaluation of geophysical data, well logs, and drill core samples. In *The Cretaceous-Tertiary Event and Other Catastrophes in Earth History* (eds. G. Ryder, D. E. Fastovsky and S. Gartner). Geological Society of America Special Paper 307, Boulder, Colorado, pp. 55–74.

Shukolyukov A. and Lugmair G. W. (1998) Isotopic evidence for the Cretaceous-Tertiary impactor and its type. *Science* **282**, 927–930.

Simpson S. L., Osinski G. R., Longstaffe F. J., Schmieder M. and Kring D. A. (2020) Hydrothermal alteration associated with the Chicxulub impact crater upper peak-ring breccias. *Earth Planet. Sci. Lett.* **547**(116425), 12p.

Smit J. (1999) The global stratigraphy of the Cretaceous-Tertiary boundary impact ejecta. *Annu. Rev. Earth. Planet. Sci.* **27**, 75–113.

Smit J. and Hertogen J. (1980) An extraterrestrial event at the Cretaceous-Tertiary boundary. *Nature* **285**, 198–200.

Son T. H. and Koeberl C. (2005) Chemical variation within fragments of Australasian tektites. *Meteorit. Planet. Sci.* **40**, 805–815.

Sprain C. J., Renne P. R., Clemens W. A. and Wilson G. P. (2018) Calibration of chron C29r: New high-precision geochronologic and paleomagnetic constraints from the Hell Creek region, Montana. *Geol. Soc. Am. Bull.* **130**, 1615–1644.

Swisher C. C., Grajales-Nishimura J. M., Montanari A., Margolis S. V., Claeys P., Alvarez W., Renne P., Cedillo-Pardoa E., Maurrasse F. J.-M. R., Curtis G. H., Smit J. and McWilliams

M. O. () Coeval $^{40}Ar/^{39}Ar$ ages of 65.0 million years ago from Chicxulub crater melt rock and Cretaceous-Tertiary boundary tektites. *Science* **257**, 954–958.

Tagle R. and Berlin J. (2008) A database of chondrite analyses including platinum group elements, Ni Co, Au, and Cr: Implications for the identification of chondritic projectiles. *Meteorit. Planet. Sci.* **43**, 541–559.

Tagle R. and Hecht L. (2006) Geochemical identification of projectiles in impact rocks. *Meteorit. Planet. Sci.* **41**, 1721–1735.

Tagle R., Erzinger J., Hecht L., Schmitt R. T., Stöffler D. and Claeys P. (2004) Platinum group elements in impactites of the ICDP Chicxulub drill core Yaxcopoil-1: Are there traces of the projectiles? *Meteorit. Planet. Sci.* **39**, 1009–1016.

Trinquier A., Birck J. L. and Allègre C. J. (2006) The nature of the KT impactor. A ^{54}Cr reappraisal. *Earth Planet. Sci. Lett.* **241**, 780–788.

Tuchscherer M. G., Reimold W. U., Koeberl C. and Gibson R. L. (2004a) Major and trace element characteristics of impactites from the Yaxcopoil-1 borehole, Chicxulub structure, Mexico. *Meteorit. Planet Sci.* **39**, 955–978.

Tuchscherer M. G., Reimold W. U., Koeberl C., Gibson R. L. and de Bruin D. (2004b) First petrographic results on impactites from the Yaxcopoil-1 borehole, Chicxulub structure, Mexico. *Meteorit. Planet. Sci.* **39**, 899–930.

Tuchscherer M. G., Reimold W. U., Koeberl C. and Gibson R. L. (2005) Geochemical and petrographic characteristics of impactites and Cretaceous target rocks from the Yaxcopoil-1 borehole, Chicxulub impact structure, Mexico: Implications for target composition. *Meteorit. Planet. Sci.* **40**, 1513–1536.

Tuchscherer M. G., Reimold W. U., Gibson R. L., de Bruin D. and Späth A. (2006) Major and trace element compositions of melt particles and associated phases from the Yaxcopoil-1 drill core, Chicxulub impact structure, Mexico. *Meteorit. Planet. Sci.* **41**, 1361–1379.

Urrutia-Fucugauchi J., Marin L. and Trejo-Garcia A. (1996) UNAM scientific drilling program of Chicxulub impact structure-Evidence for a 300 kilometer crater diameter. *Geophys. Res. Lett.* **23**, 1565–1568.

Urrutia-Fucugauchi J., Camargo-Zanoguera A., Perez-Cruz L. and Perez-Cruz G. (2011) The Chicxulub multi-ring impact crater, Yucatan carbonate platform, Gulf of Mexico. *Geofis. Int.* **50**, 99–127.

Vermeesch P. (2018) IsoplotR: a free and open toolbox for geochronology. *Geosci. Front.* **9**, 1479–1493.

Völkening J., Walczyk T. and Heumann K. G. (1991) Osmium isotope ratio determinations by negative thermal ionization mass-spectrometry. *Int. J. Spectrom. Ion Process.* **105**, 147–159.

Wallace M. W., Gostin V. A. and Keays R. R. (1990) Acraman impact ejecta and host shales: Evidence for low-temperature mobilization of iridium and other platinoids. *Geology* **18**, 132–135.

Walker J. W., Prichard H. M., Ishiwatari A. and Pimentel M. (2002) The osmium isotopic composition of convecting upper mantle deduced from ophiolite chromites. *Geochim. Cosmochim. Acta* **66**, 329–345.

Ward W. C., Keller G., Stinnesbeck W. and Adatte T. (1995) Yucatán subsurface stratigraphy: Implications and constraints for the Chicxulub impact. *Geology* **23**, 873–876.

Whalen M. T., Gulick S. P. S., Lowery C. M., Bralower T. J., Morgan J. V., Grice K., Schaefer B., Smit J., Ormö J., Wittmann A., Kring D. A., Lyons S., Goderis S. and IODP-ICDP Expedition 364 Scientists (2020) Winding down the Chicxulub impact: The transition between impact and normal marine sedimentation near ground zero. *Mar. Geol.* **430** 106368.

Wimpenny J., Gannoun A., Burton K. W., Widdowson M., James R. H. and Gislason S. R. (2007) Rhenium and osmium isotope and elemental behaviour accompanying laterite formation in the Deccan region of India. *Earth Planet. Sci. Lett.* **261**, 239–258.

Xie X., Yan M., Wang C., Li L. and Shen H. (1989) Geochemical Standard Reference Samples GSD 9–12, GSS 1–8 and GSR 1–6. *Geostandards Newslett.* **13**, 83–179.

Zhao J., Xiao L., Gulick S. P. S., Morgan J. V., Kring D. A., Urrutia-Fucugauchi J., Schmieder M., de Graaff S. J., Wittmann A., Ross C. H., Claeys P., Pickersgill A., Kaskes P., Goderis S., Rasmussen C., Vajda V., Ferrière L., Feignon J.-G., Chenot E., Perez-Cruz L., Sato H., Yamaguchi K. and IODP-ICDP Expedition 364 Scientists (2020) Geochemistry, geochronology and petrogenesis of Maya Block granitoids and dykes from the Chicxulub Impact Crater, Gulf of México: Implications for the assembly of Pangea. *Gondwana Res.* **82**, 128–150.

Associate editor: Marc Norman